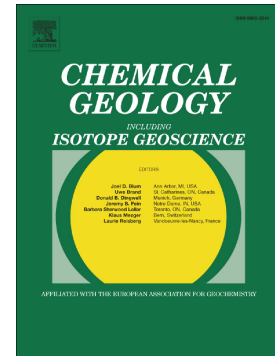


Accepted Manuscript

Depositional and diagenetic constraints on the abundance and spatial variability of carbonate-associated sulfate

Jocelyn A. Richardson, Matthew Newville, Antonio Lanzirotti, Samuel M. Webb, Catherine V. Rose, Jeffrey G. Catalano, David A. Fike



PII: S0009-2541(19)30268-2
DOI: <https://doi.org/10.1016/j.chemgeo.2019.05.036>
Reference: CHEMGE 19195
To appear in: *Chemical Geology*
Received date: 14 November 2018
Revised date: 23 May 2019
Accepted date: 29 May 2019

Please cite this article as: J.A. Richardson, M. Newville, A. Lanzirotti, et al., Depositional and diagenetic constraints on the abundance and spatial variability of carbonate-associated sulfate, *Chemical Geology*, <https://doi.org/10.1016/j.chemgeo.2019.05.036>

This is a PDF file of an unedited manuscript that has been accepted for publication. As a service to our customers we are providing this early version of the manuscript. The manuscript will undergo copyediting, typesetting, and review of the resulting proof before it is published in its final form. Please note that during the production process errors may be discovered which could affect the content, and all legal disclaimers that apply to the journal pertain.

**Depositional and Diagenetic Constraints on the Abundance and Spatial Variability of
Carbonate-Associated Sulfate**

Jocelyn A. Richardson^{1*}, Matthew Newville², Antonio Lanzirotti², Samuel M. Webb³, Catherine
V. Rose⁴, Jeffrey G. Catalano¹ and David A. Fike^{1*}

¹Department of Earth and Planetary Sciences, Washington University, St. Louis, MO 63130 USA

²Consortium for Advanced Radiation Sources University of Chicago, Chicago, IL 60637, USA

³Stanford Synchrotron Radiation Lightsource, Menlo Park, CA 94025, USA

⁴School of Earth and Environmental Sciences, University of St Andrews, Fife KY16 9AL, UK

*Corresponding authors:

E-mail: j.richardson@wustl.edu. Phone: +1 (314) 935-8206

E-mail: dfike@levee.wustl.edu. Phone: +1 (314) 935-6607

Declarations of interest: none

ACCEPTED MANUSCRIPT

Abstract

Marine carbonate rocks are composed, in varying abundance, of cement, micrite, abiotic grains and fossils, which can provide information about the physical and chemical environments in which they formed. Geochemical analyses of these carbonates are not always interpreted alongside the wealth of geologic (including petrographic) information available, resulting in potentially faulty reconstructions of biogeochemical and environmental conditions. These concerns have prompted closer scrutiny of the effect of depositional lithofacies and diagenesis on carbonate proxies. Here, we have combined X-ray Absorption Near Edge Structure (XANES) spectroscopy and μ -X-ray Fluorescence (μ -XRF) imaging to map the speciation and abundance of sulfur in carbonate petrographic thin sections in Upper Ordovician carbonates from Anticosti Island, Canada and early Silurian carbonates from Gotland, Sweden, across multiple depositional facies. Lithofacies and fossil communities between Anticosti Island and Gotland are similar, which allows for comparison of changes in the dominant S species and their abundance in separate basins, associated with variations in (glacio)eustatic sea level. Sulfide abundance is greatest in mudstone, wackestone and packstone facies, where interstitial micrite hosts abundant pyrite. Sulfate abundance, as carbonate-associated sulfate (CAS), varies within individual fossil fragments, as well as within the same fossil phylum and is particularly high in unaltered brachiopods. In contrast, sulfate abundance is generally very low in micrite (near the detection limit) and generally arises in situ from sulfide that has been oxidized as opposed to true CAS. In different cement fabrics, sulfate abundance is greatest in drusy, pore-filling cements. Organic sulfur compounds are also detected and, although low in abundance, are mostly found within micrite. The detection and characterization of both inorganic sulfur and organic sulfur compounds provides a platform to understand early processes of biomineralization. This

approach will broaden our understanding of the source of inorganically bound sulfate in ancient carbonates, as well as the effect of depositional setting and diagenesis on CAS incorporation, (re)mobilization, and ultimate abundance in sedimentary carbonates. Additionally, this work has implications for the CAS isotopic value of individual carbonate components that may affect interpretations of stratigraphic variability of numerous CAS sections throughout Earth history.

Keywords: carbonate-associated sulfate; XANES spectroscopy; μ -XRF imaging; diagenesis; depositional environment; sulfur isotopes

1.0 Introduction

Over geologic timescales, the marine sulfur cycle is closely linked to the redox state of the Earth's surface environments due to the relative burial ratio between the redox-sensitive sulfur species (i.e. sulfide and sulfate) (Berner and Raiswell, 1983). As a result, carbonate rocks are frequently analysed for the abundance and isotopic composition ($\delta^{34}\text{S}$) of their S-bearing phases, primarily pyrite and carbonate-associated sulfate (CAS), to understand long-term trends in sulfur cycling (Canfield, 2004; Fike and Grotzinger, 2008). CAS is used as a proxy for the composition of ancient seawater sulfate, understood to reflect the ambient incorporation and substitution of a sulfate ion for a carbonate ion during carbonate precipitation (Burdett et al., 1989). Given the large extent of carbonate precipitation throughout Earth history, many studies have used CAS to generate high-resolution datasets to constrain the operation and temporal evolution of the marine S-cycle from the Archean to the Cenozoic (Burdett et al., 1989; Crowe et al., 2014; Fike and Grotzinger, 2008; Gill et al., 2007; Hurtgen et al., 2009; Jones and Fike, 2013; Kampschulte and

Strauss, 2004; Kozik et al., 2019; Osburn et al., 2015; Ries et al., 2009; Thompson and Kah, 2012; Turchyn et al., 2009).

Unlike many other geochemical proxies that are a major component of carbonates (such as $\delta^{13}\text{C}_{\text{carb}}$), CAS is a trace component, where abundances typically range from tens to hundreds of ppm in ancient carbonates and hundreds to thousands of ppm in modern carbonates (Staudt and Schoonen, 1995). These low abundances in ancient rocks indicate CAS may be more susceptible to alteration than other proxies (e.g., $\delta^{13}\text{C}$), which may contribute to the characteristic sample-to-sample isotopic variability (as much as 10‰; e.g. Edwards et al., 2018; Jones and Fike, 2013; Riccardi et al., 2006) observed in $\delta^{34}\text{S}_{\text{CAS}}$ in many deep-time records (Kampschulte and Strauss, 2004; Osburn et al., 2015; Rose et al., 2019). Such high-frequency stratigraphic variability cannot be accounted for by changes to the global marine sulfate reservoir, due to the multi-million-year residence time of seawater sulfate (Berner, 2001).

Carbonates can be composed, in varying abundances, of four major components; micrite (microcrystalline calcite or 'lime mud'), cement, fossils and abiotic grains, all of which can be differentially affected by diagenesis. Diagenesis of carbonates includes any process occurring after the precipitation/sedimentation of carbonate, including lithification. Examples of diagenetic fluids that may affect marine carbonates are: (chemically evolved) porewaters, meteoric fluids, dolomitizing fluids, and basinal brine fluids. Several studies have assessed the effect of diagenesis on CAS of bulk rock samples (Fichtner et al., 2017; Gill et al., 2008; Hurtgen et al., 2006; Rennie and Turchyn, 2014; Richardson et al., 2019). Others have attempted to reduce the effect of secondary CAS signals by selecting for individual carbonate phases (e.g. micrite and brachiopods in Kampschulte and Strauss, 2004; Wotte et al., 2012a; fossils in Gill et al., 2011; Kampschulte et al., 2001; Present et al., 2015), and/or by reducing sample size to minimize the

number of altered components homogenized into the sample (Paris et al., 2014; Present et al., 2015; Rennie et al., 2018). Additionally, an increasing number of studies are emphasising the potential impact that sedimentary facies, and therefore relative local sea level, have on CAS abundance, $\delta^{34}\text{S}_{\text{CAS}}$, and $\delta^{34}\text{S}_{\text{pyr}}$ preserved in the rock record (Fike et al., 2015; Pasquier et al., 2017; Richardson et al., 2019; Rose et al., 2019; Strauss, 1997). Depositional environments can affect the relative abundance of carbonate components, producing lithofacies (outcrop and hand sample observations) and microfacies (petrographic observations) that likely have their own imprint on the initial composition of CAS.

Until recently, it was unknown how CAS abundance varied spatially within an individual hand sample (Present et al., 2015; Rose et al., in review). Due to the low abundance of CAS in the rock record, there have been few techniques that can determine the CAS abundance of individual components within a petrographic context. Micro X-Ray Fluorescence (μ -XRF) imaging and X-Ray Absorption Near Edge Structure (XANES) spectroscopy make possible the non-destructive detection of low abundance S-species at micrometer-scale spatial resolution within a petrographic context. S-species have a wide range of oxidation states that corresponds to ~14 eV range of absorption edge energies in XANES spectroscopy (Hedman et al., 1986), providing an ideal platform for multi-energy μ -XRF imaging that can distinguish among the various S species. Coordination with petrographic observations allows for identification of primary and diagenetic components. Initial investigations by Rose et al. (in review) indicate sulfate abundance is spatially variable within an individual Ordovician carbonate thin section, with CAS abundance ranging from ~10 to 200 ppm. The study identified multiple sulfate moieties using XANES spectroscopy, showing that sulfate is present both as organic esters and in two inorganic phases, each likely associated with distinct carbonate lattice structures. The

present study expands on this earlier work by combining petrographic observations, μ -XRF imaging, and XANES spectroscopy on multiple samples from a range of lithofacies from Anticosti Island, Canada and Gotland, Sweden (Fig. 1). The samples from these localities were chosen as they span critical periods of Earth history with known biological turnover (End-Ordovician mass extinction and the mid-Silurian Ireviken Bioevent; IBE), climate change, glacioeustatic sea level change and well-documented perturbations to the global carbon cycle. These samples are well characterized in terms of broad sedimentology and stratigraphy, geochemistry and bulk carbon and sulfur isotopes (Jones and Fike, 2013; Present et al., 2015; Rose et al., 2019). This approach assesses the dominant sulfur species and how they vary among lithofacies and between primary and diagenetic carbonate phases. We present a subset of μ -XRF images and XANES spectra from Ordovician and Silurian carbonate samples that we have generated.

Here we show a model for the source, incorporation and preservation of S-species in primary carbonate (fossils), the source and preservation of sulfur during lithification and early diagenesis (formation of cement and micrite), and the fate of the S-species during post-depositional, late-stage alteration (e.g., replacement of fossils, carbonate mineral neomorphism). Such insights at the micron scale will aid our understanding and interpretations of bulk chemostratigraphic data, where biogeochemical proxies ultimately may reflect local, facies-dependent controls superimposed on any basinal or global signatures.

2.0 Materials and Methods

Anticosti Island, Quebec, Canada (Fig. 1), represents a storm-dominated carbonate platform, with 200 km of E-W trending, well-exposed strata that has experienced minimal structural

deformation. Strata on the north of Anticosti are Hirnantian, ~ 444 Ma, and young to the south (Desrochers et al., 2010; Long and Copper, 1987). The Ordovician and Silurian carbonate rocks on Anticosti Island dip to the south west and have been buried to depths within the oil window (Desrochers et al., 2010; Jones et al., 2011; Pinet and Lavoie, 2007). Late-stage diagenesis and fluid migration has not appreciably affected the abundance and isotopes of sulfate or sulfide (Jones and Fike, 2013). Samples in this study from Anticosti span a range of shallow-water carbonate lithofacies corresponding to the latest Hirnantian, associated with the end-Ordovician mass extinction, a well-documented global C-isotope excursion, and glaciation that is expressed as a shallowing-upward facies transition (Jones et al., 2011; Jones and Fike, 2013). The samples presented are sourced from the Lousy Cove and Laframboise members of the Ellis Bay Formation, from Laframboise point (section 901) and Salmon River (section 908) (Fig 1b; Jones et al., 2011).

Gotland, Sweden (Fig. 1), represents numerous stacked carbonate platforms that formed in the Baltoscandian basin during the Silurian. Strata are the oldest in the northwest of Gotland, with progressively younger strata to the south. The carbonate strata on Gotland are minimally thermally and tectonically altered (Jeppsson, 1983) and bulk geochemistry shows little broad-scale resetting of isotope proxies (Rose et al., 2019). Here, Gotland samples are from the early Wenlock (~ 428 Ma) and consist of shallow-water carbonates that span the Ireviken Bioevent (IBE) and a well-defined global C-isotope excursion coincident with a facies change that represents marine regression and a cooling climate (Lehnert et al., 2010; Munnecke et al., 2010, 2003). The samples were sourced from numerous sections along the northern edge of Gotland from the Lower Visby, Upper Visby and Tofa formations (sections G1, G4 and G7; Fig. 1c; Rose et al., 2019).

Synchrotron analyses were performed around the S K-edge (2472 eV) conducted at the GeoSoilEnviroCARS (GSECARS) beamline 13-ID-E at the Advanced Photon Source (APS) at Argonne National Laboratory and beamline 14-3 at the Stanford Synchrotron Radiation Lightsource (SSRL), SLAC National Accelerator Laboratory. Detailed beamline configurations and measurement approaches have been described previously (Rose et al., in review). Both the APS 13-ID-E and SSRL 14-3 beamlines utilize grazing incidence, silicon mirror focusing for μ -XRF and XANES data collection. At both facilities, the sample environment is a helium-purged chamber. The detectors are different at each beamline (Vortex ME-4 silicon drift-diode detector array at APS and Vortex silicon drift diode detector 97 at SSRL), which could impact the sensitivity in measuring S. The apparent S K-edge differs slightly between APS and SSRL, likely due to monochromator calibration. There were differences in data collection because of distinct facility characteristics. At APS, the energy was calibrated using a CaSO_4 standard that provides a maximum intensity white line at ~ 2481.5 eV. For the APS analyses, the pitch of the focusing mirrors was slightly decreased, thus, the monochromatized X-ray beam contained a small component of 3rd order harmonic (i.e., X-ray photons with energies near 7500 eV). This adjustment allowed for the ability to generate spatial distribution maps of elements with absorption edges higher than that of the S K-edge at ~ 2472 eV (e.g. Mn, Fe). At the APS, maps representative of the distribution of sulfide and sulfate were generated by collecting data at energies corresponding to the highest absorption for each species (2471 eV and 2482 eV respectively; Fig. 2). Maps of total sulfur were also generated at 2550 eV, well above the absorption edge energy. As part of the data correction, sulfide fluorescence that occurred when mapping at the sulfate excitation energy has been removed from all of the sulfate energy maps presented here (using the MicroAnalysis Toolkit (Webb et al., 2011) and GSE Mapviewer

(Newville, 2013)). All maps are normalized to the edge-step and are scaled to the same total S counts, such that the white pixels on each map that represent maximum counts, correspond to the same number of counts across each map. XANES spectra were collected at the APS to verify sulfur speciation at locations identified during mapping.

The optics at SSRL BL 14-3 were tuned to reduce higher-order harmonics, so only S-species were imaged. The energy was calibrated to the S K-edge at 2472.2 eV using a sodium thiosulfate powder. Maps were collected at more energies to allow for detection and differentiation of less abundant S-species and structural changes to the sulfate ion. Multi-energy maps were collected at 2472, 2476.3, 2482.1, 2482.3, 2482.5, 2482.65, 2482.8 and 2483.2 eV in order to distinguish subtle differences in the K-edge spectra of sulfate moieties. A greater number of XANES spectra were collected on each mapped region at SSRL (Sixpack; Webb, 2005). A principal component analysis was performed on the XANES dataset from each region. Using these analyses, component score plots (where one component is plotted against another component) were used to identify the XANES spectra that are the most different from one another, but together encompass the entire variation of the XANES dataset for the given region. Spatial distribution maps of the energy of maximum intensity in the end-member XANES spectra, such as co-occurring sulfide and sulfate or organic sulfur compounds (OSCs), are generated by performing a least-squares XANES fitting of the end-member spectra to the original multi-energy maps (Mayhew et al., 2011). That is, the normalized fluorescence intensity of a given end-member spectra is determined for each of the multi-energies that was mapped. A least-squares fitting of the normalized fluorescence intensity is applied to each pixel using the data collected at the same pixel in the multi-energy map, generating an abundance map of the given end-member spectrum.

3.0 Results

3.1 Fossils and Grains

Fossils show variation in sulfate abundance between different phyla or classes (Fig. 3), as well as within certain phyla (e.g. brachiopods, Fig. 4c and 4d). Abiotic grains also differ in sulfate abundance between grains as seen in Figs. 3b and 3c, which correspond to different locations within the same thin section. These regions were mapped consecutively during the same analytical session so there were no differences in beam characteristics. During the Ordovician and Silurian, the major reef builders were tabulate (e.g. *Coenites sp.*, C in Fig. 3a) and rugose corals (RU; Fig. 3c), and stromatoporoids. Other important biomineralizers include brachiopods (B; Fig. 4d), bryozoans (BRY; Fig. 4a), crinoids (Fig. 5a) and ostracods (Scholle and Ulmer-Scholle, 2003). Bivalves and gastropods make up a large proportion of unidentified fossil fragments throughout the Phanerozoic, evident in the Ordovician grainstone samples studied here (Fig. 3b and 3c).

Tabulate and rugose corals are present in all studied packstone and grainstone facies from Anticosti Island and Gotland. Corals in these samples always consist of both micrite, from infilling or micritization, and recrystallized calcite (Figs. 3a and 3c). *Coenites sp.* (Fig. 3a) is a branching tabulate coral that makes up the centre of oncoids in a poorly washed fossiliferous grainstone from the Upper Visby Formation on Gotland (platform interior shoal facies). In this sample, *Coenites sp.* is associated with *Allonema sp.*, a calcareous encrusting problematica (Jarochowska and Munnecke, 2014) (Fig. 3a, inset), forming an oncoid. *Allonema sp.* is predominantly preserved as micrite, with small recrystallized vesicles of the original *Allonema* structure. The main S-species in the micrite of *Allonema sp.* is sulfide (Fig. 3d, XANES

spectrum 5) as well as the detection of thiol (XANES spectrum 4). The recrystallized vesicles within the micrite show localized increases in sulfate content (Fig. 3a and 3d, XANES spectrum 1). These vesicles lack sulfide but do contain low abundances of thiol/thioether and sulfite (2473.2 and 2477.8 eV respectively) (Almkvist et al., 2010). Variation in the intensity of the thiol/thioether and sulfite peak occurs within the micrite in the centre of *Coenites sp.* (Fig. 3a and 3d, XANES spectra 2 and 3).

The oncolite grainstone from the La Framboise Member on Anticosti Island (Fig. 1b), deposited in the platform interior as coarse reef-debris facies, contains high proportions of bioclast fragments and lithoclasts that show strong variations in sulfate abundance across the sample (Fig. 3b and 3c). Bioclasts are commonly recrystallized (RC), surrounded by micritic envelopes (ME), or fully micritized (MB; Fig. 3b and 3c). Micritic lithoclasts (M), micrite envelopes, and micritized bioclasts frequently contain signals from both sulfide and sulfate within a given location (Fig. 3d XANES spectra 8 and 11). Additionally, XANES spectroscopy detects a subtle shift in the maximum energy of the inorganic sulfate peak from 2482.3 to 2482.6 eV between different bioclast fragments in the oncolite grainstone (Figs. 3b and 3d, XANES spectra 6, 7 and 9). Fig. 3c hosts a large solitary rugose coral (RU) where the fossilized calyx and septa are micrite, and the dissepiments are filled with recrystallized calcite. The sulfate abundance is greatest in the preserved skeleton, now micrite, whereas sulfate abundance is very low in the recrystallized dissepiments. The micrite in the mold of the rugose coral contains strong signals for inorganic sulfate, consistent with CAS, with no interference from sulfide. Brachiopods contain the highest concentration of sulfate of all fossils studied (Figs. 4c and 4d), whereas well-preserved bryozoans also contain high abundances of sulfate (Fig. 4a).

3.2 Cement

Sulfides are generally less abundant in cement when compared to micrite (Fig. 4 vs. Fig. 5). Fig. 4 depicts a variety of cements from packstone and grainstone facies. The microfacies of the Lousy Cove Member of the Hirnantian-aged Ellis Bay Formation on Anticosti Island (Fig. 1b and 4a; Jones et al., 2011) indicate formation on the platform interior in an open marine environment. Similarly, the Lower Visby, Tofta and Hogklint formations of Gotland during the early Wenlock have platform interior (reef) and margin microfacies (Figs. 1c, 4b, c and d). These samples (both Anticosti and Gotland) are from the rising limb of the C-isotope excursions at each locality, coincident with a lithofacies change reflecting marine regression.

Sulfate abundance in equant, blocky cement (BL) is usually near the detection limit (Fig. 4a), although abundance is sometimes observed to increase at crystal boundaries. Syntaxial calcite overgrowths (SO), single calcite crystal overgrowths around a pre-existing grain (Fig. 4b), are commonly formed over echinoderm fragments (here crinoid fragments) of high-Mg calcite (Christ et al., 2015; Flügel and Munnecke, 2010). The sulfate abundance in syntaxial cement varies relative to the crinoid fragment underneath (Fig. 4b showing both lower abundance (right) and similar or greater abundance (left) of sulfate). Drusy cements (DR) are characteristically pore-filling cements where the crystal size of the cement increases towards the center of the pore (Flügel and Munnecke, 2010; Figs. 4c and 4d). Drusy cements are observed here to have higher sulfate concentrations than blocky cements; further, the CAS abundances increase toward the center of these cements.

3.3 Micrite

Micrite is fine-grained carbonate and is a major interstitial component of mudstone, wackestone, and packstone facies. Micrite contains the highest abundance of sulfide compared to the other carbonate components. Fig. 5a is a wackestone from the Lousy Cove Member on Anticosti Island (Fig 1b). Microfacies observations indicate that the depositional environment was a shallow platform-margin reef. The sulfide map (Fig. 5b) shows finely disseminated sulfide throughout the micrite, and to a lesser extent within the micritized crinoid fragments. This sulfide is observed in all samples analysed that have interstitial and micritized fossil fragments, and is mostly pyrite, determined through a correlation with Fe abundance maps and XANES spectra. In addition, there are isolated sulfates phases within the micrite (Fig. 5c). Moreover, a majority of the sulfides have been partially oxidized, contributing to the sulfate signal (Fig. 5d), which is confirmed by XANES spectroscopy, showing both sulfide and sulfate peaks present at one location (Fig. 5e). The intensity of co-occurring sulfide and sulfate peaks vary, indicative of differing amounts of oxidation across the sample. There are few spectra from this region with a sulfate signal without accompanying sulfide, and, where they do occur, they are associated with a low sulfate background within crinoid fragments (Fig. 5e, location 5). Micrite is also present in grainstone samples, where it is observed in lithoclasts, oncolitic and cortoid grains as micritic envelopes, and calcareous algae and cyanobacteria, where again sulfides are abundant.

4.0 Discussion

4.1 Sulfate in Primary Carbonate

Primary carbonate components are those that precipitate within seawater, or within sediment that is in open connectivity with seawater (e.g. deep-water facies; Claypool, 2004; Richardson et al., 2019). Relatively little is known about the biological incorporation of sulfate

into carbonate, and whether the mechanism is ambient incorporation, akin to that for inorganic carbonate (Busenberg and Plummer, 1985; Staudt et al., 1994), or if there is a biological control and/or source during incorporation (Burdett et al., 1989; Cuif et al., 2003; Cusack et al., 2008; Yoshimura et al., 2013). The majority of carbonate cementation occurs in the subsurface, usually within the first few mm (Flügel and Munnecke, 2010). Although some carbonate may precipitate directly on the seafloor, there is no evidence for seafloor encrustations in these samples. The origin and formation of micrite can occur via multiple pathways: authigenic precipitation within the water column or in the sediment (automicrite), physical or chemical breakdown of skeletal fragments or calcareous algae (allomicrite), and diagenetically through recrystallization (diagenetic micrite and microspar; Flügel and Munnecke, 2010). As such, fossils are the only component derived directly from local ambient seawater in these samples and we, thus, focus our discussion of sulfate variability in preserved primary fossil fabrics. The fate of sulfate during diagenesis of primary carbonate (e.g. micritization of fossils) is discussed in sections 4.2 and 4.3.

Few fossils retain their primary carbonate mineralogy and fabric over geologic time. Brachiopods, however, are commonly robust to recrystallization owing to the multi-layered low-Mg calcite shell of articulate brachiopods (Lowenstam, 1961). The abundance of sulfate within brachiopod shells is the highest of all components analysed. The sulfate abundance appears banded, correlating to the primary brachiopod structure (Figs. 4c and 4d) where calcite crystals are oriented obliquely to the shell edge. Such high-resolution mapping of sulfate within brachiopods has not been shown before. In the extant brachiopod *Terebratulina retusa*, sulfate abundance is greatest in the primary (outer) layer of the shell coincident with increased Mg abundance and, although sulfate is present in the secondary fibrous layer, it is lower in abundance and is surrounded by thiols (Cusack et al., 2008). This prior work was unable to

determine if sulfate-bearing polysaccharides were the source of the sulfate in the primary layer or what contributed to differences in the sulfate abundance between the primary and secondary layers. Here, we are unable to differentiate between the primary and secondary layers in the petrographic thin sections. However, the μ -XRF maps do not show gradients across the shell in sulfate abundance, implying that these species do not contain obvious differences between the primary and secondary layers, that and differences are not resolvable at this scale, or that the primary layer in these specimens was not preserved. XANES spectra within the brachiopods indicate that inorganic sulfate comprises the vast majority of sulfate. It has been suggested that brachiopods may preserve a more faithful record of CAS abundance and $\delta^{34}\text{S}_{\text{CAS}}$ due to the resistance of the primary brachiopod shell structure to recrystallization (Kampschulte and Strauss, 2004; Present et al., 2015). The detailed preservation of brachiopods here, combined with the maps showing sulfate variability within the shell fabric and XANES spectra characteristic of inorganic sulfate, indicate that brachiopods could be an archive of primary CAS.

Like brachiopods, well-preserved bryozoans contain a high abundance of sulfate (Fig. 4a). There are few previous studies of CAS in bryozoans, but extant bryozoans contain > 5000 ppm sulfate (Staudt and Schoonen, 1995) and micro-drilling of Ordovician-aged bryozoans from Anticosti Island indicates that their sulfate content is ~500 ppm, within a similar range of coeval brachiopods (Present et al., 2015). The detailed preservation of the bryozoan, and its sulfate content, suggests this may also be a potentially primary sulfate signal (Fig. 4a). Fossil bryozoa, especially those from the family Stenolaemata (common in Ordovician and Silurian carbonate strata; Ernst and Munnecke, 2009) form their exoskeleton from low-Mg calcite. This could mean that fossil bryozoan, like brachiopods, are similarly robust to diagenetic recrystallization (Smith et al., 2006). However, the observed difference in magnitude in concentration between extant

and fossil bryozoans could indicate partial loss of sulfate during diagenesis, perhaps pertaining to greater porosity and permeability of bryozoan exoskeletons when compared to brachiopods. This difference in sulfate requires further investigation, including isotopic studies, to determine whether bryozoans may be a faithful archive of CAS, that can corroborate brachiopod evidence, or provide data where brachiopods are absent. Generally, all other fossils in these samples have been replaced by micrite and/or cement, where the sulfate abundance may be compromised by post-depositional alteration.

4.2 Lithification and Early Marine Diagenesis

Carbonate cementation is an essential part in lithification and studying the resulting cements can be informative about their history of formation and subsequent diagenesis due to the variety of morphologies and fabrics formed. Equant blocky fabrics (Fig. 4a) suggest there was recrystallization of pre-existing cement in meteoric or burial environments (Flügel and Munnecke, 2010). The low sulfate concentration in the cement in Fig. 4a indicates that the diagenetic fluid causing recrystallization must also have been low in sulfate, such as meteoric or sulfate-poor porewaters, likely precluding a basinal fluid. Fe and Mn abundance maps do not show elevated abundance in the cements (Fig. 6), which are anticipated to increase during recrystallization in contact with anoxic fluids (Brand and Veizer, 1980). Sedimentary porewaters may evolve under closed-system conditions, where sulfate in the porewater is used up by microbial sulfate reduction (MSR) more rapidly than it is replenished by diffusion from the overlying seawater. Such closed-system conditions occur preferentially in shallow-water environments due to increased sedimentation rates and increased labile organic carbon and Fe abundance (Aller et al., 2010; Fike et al., 2015; Toth and Lerman, 1977). Together these

observations indicate that equant cements formed below the region where porewaters retained substantial sulfate or precipitated at a slow enough rate that resulted in inefficient incorporation of sulfate into the carbonate lattice (Busenberg and Plummer, 1985; Kile et al., 2000).

‘Cloudy’ syntaxial cement is indicative of meteoric or early, shallow marine diagenesis (Walker et al., 1990) (Fig. 4b). Due to the moderate abundance of sulfate, meteoric diagenesis is deemed unlikely, thus the formation of the syntaxial overgrowth is likely early diagenetic. Sulfate abundance in the syntaxial cement is usually greater than the blocky cement in Fig. 4a. The higher abundance of sulfate in the syntaxial overgrowth could reflect the resupply of porewater sulfate for example, by tidal pumping (Aller et al., 2010) and/or faster rates of crystal growth. A tidal influence is consistent with thin-section observations of a change to smaller and more abundant fossil fragments and an increase in lithoclasts associated with the presence of syntaxial overgrowths.

During the Ordovician and Silurian, drusy pore-filling cements are commonly of early marine origin (Figs. 4c and 4d) (Christ et al., 2015) due to the lower Mg/Ca ratio of seawater causing more rapid growth along the *a* and *b* crystallographic axes, resulting in complex polyhedral crystal habits (Folk, 1965). Evolution of the sulfate concentration in porewater is likely to occur as a result of progressive MSR, where $[\text{SO}_4^{2-}]$ decreases with increasing depth in the sediment (Fig. 7). MSR increases alkalinity, and ultimately encourages carbonate precipitation in pore spaces with depth in the sediment (Baumgartner et al., 2006; Berner et al., 1970). Increased carbonate supersaturation in turn causes an increase in the rate of carbonate precipitation (Langdon et al., 2000). Busenberg and Plummer (1985) found that the rate of carbonate growth increases the distribution coefficient of sulfate into calcite, i.e. as the rate of crystal growth increases, so does the amount of sulfate substituted into the mineral. Thus, in a

setting of increased and more rapid calcite precipitation, CAS abundance should increase (in accordance with Busenberg and Plummer, 1985). However, CAS abundance should also scale with $\text{SO}_4^{2-}:\text{CO}_3^{2-}$ ratio. As such, for CAS abundance to increase as MSR decreases SO_4^{2-} availability, the rate of precipitation would need to be sufficient to offset the decreasing $\text{SO}_4^{2-}:\text{CO}_3^{2-}$ ratio.

The variability in CAS within single crystals of drusy cements can be explained by sector zoning. It has been demonstrated that surface topography of calcite can induce SO_4^{2-} sectoral and intra-sectoral zoning within the mineral structure (Staudt et al., 1994). The effective partition coefficient of sulfate into calcite depends on mechanistic properties of incorporation and surface structural controls (spiral growth vs. linear attachment) (Staudt et al., 1994). Thus, it is possible that cements in these thin sections have recorded and preserved structural properties during precipitation that may have affected the effective partition coefficient within a given crystal, resulting in the observed CAS variability in a single cement crystal. Although it is uncommon for studies to target only cement components, these findings have implications for bulk $\delta^{34}\text{S}_{\text{CAS}}$ records that will homogenize variable amounts of different cement morphologies based on the lithofacies, ultimately masking and/or muting the primary $\delta^{34}\text{S}_{\text{CAS}}$ signal. This is likely to contribute to the inherent variability in most ancient $\delta^{34}\text{S}_{\text{CAS}}$ records, where the changes occur too rapidly with respect to the residence time of seawater sulfate and thus cannot reflect changes to the global sulfur cycle. Although such variability may sometimes be interpreted as transient perturbations to the local sulfur cycle, our findings suggest this may also be explained by changes in the carbonate lithofacies. We anticipate such phase-specific sulfate variability is found in all carbonate rocks and the unique micron-scale environmental signatures are lost by averaging components.

Allomicrite, common in shallow-water carbonates studied here (Fig. 5), has a higher proportion of pyrite than automicrite (e.g. micrite clasts in Fig. 4b). This increase may result from an influx of organic matter during fossil breakdown, promoting MSR by increasing the availability of labile organic carbon (Leavitt et al., 2013; Sim et al., 2011). Any newly produced sulfide could form pyrite if the environment is not Fe limited. Sulfate abundance is low (< 100 ppm) in all micrite analyzed. This observation could be due to the sulfate-limited environment resulting from increased MSR and/or a result of the generally high abundance of silicate minerals and Fe within micrite (Rose et al., in review), essentially diluting the abundance of sulfate contained within the fine-grained fossil fragments. The high abundance of sulfide present in micrite is most likely an observation that will apply to micrite precipitated in various locations throughout Earth History. We suggest this high abundance of sulfide is due to the increased surface area where there may be increased availability of iron and organics (to fuel MSR) due to surface sorption.

4.3 Post-depositional Alteration

Unfortunately, there are currently no good constraints to determine the exact timing of formation of interstitial micrite and cements. As such, we limit discussion of post-depositional alteration to fossil micritization and recrystallization, replacement fabrics of cements, and oxidation of sulfide. Primary carbonate fabrics are commonly replaced in many bioclast fragments via micritization by algae or dissolution and re-precipitation of cement. Multiple secondary textures may be found within a single fossil: for example, the fossilized calyx and septa of the rugose coral in the Anticosti Island oncolite grainstone are micrite and the dissepiments contain recrystallized calcite (Fig. 3c). Sulfate concentrations are highest in the

micrite and very low in the recrystallized dissepiments, indicating this latter cement formed from meteoric fluid or evolved porewater lacking substantial residual sulfate. Additional peaks in the XANES spectra of the rugose coral (and *Coenites sp.* from Gotland; Figs. 3a, 3c and 3d) indicate the presence of thiol/thioether and sulfite. This may suggest that low abundances of primary S-species were retained during dissolution of the primary carbonate due to the similarity of these spectra with prior reports (Perrin et al., 2017; Tamenori et al., 2014). However, it is possible to generate intermediate valence S compounds as the result of x-ray irradiance. Specifically, there is evidence for beam-induced reduction of sulfate to sulfite within silicate glass (Wilke et al., 2008). Due to the low intensity of the sulfite peak, photoreduction of sulfate cannot be precluded as the source of the sulfite here. Sulfite in carbonates has been detected previously, thus, the samples here are not anomalous (Frisia et al., 2005; Perrin et al., 2017). Additionally, the intensity of the sulfite peak varies within the given location (Fig. 3d XANES 1-3) and is only rarely observed. Together these observations argue that the detection of sulfide is not an artefact (Perrin et al., 2017).

XANES spectroscopy has previously been used to assess the occurrence of organic sulfur compounds (OSCs) in ancient carbonates. For example, Rose et al. (in review) document the presence of sulfate esters within a series of Upper Ordovician carbonates. Cuif et al. (2003) measure sulfate within corals and infer these to be in the form of sulfate esters. Because this sulfate dominated in the calcification centres and fibres within the septa of Scleractinian corals *Montastrea*, *Favia* and *Lophelia*, Cuif et al. (2003) infer that sulfate esters (chondroitin sulfate) are very important in the biomineralization process of these genera. However, XANES spectra in each of the Scleractinia lack the characteristic 'shoulder' (additional peak) of a sulfate ester (Almkvist et al., 2010) and look strikingly similar to XANES spectrum herein determined to be

inorganic sulfate. Dauphin et al., (2003) similarly conclude that chondroitin sulfate is present in the mollusc shells *Pinna* and *Pinctada* despite the XANES spectra lacking the shoulder of an ester sulfate. In contrast, XANES investigations of *Corallium* (Tamenori et al., 2014; Perrin et al., 2017), a deep-water coral, show inorganic sulfate and a weak sulfite signal within the calcite skeleton. XANES spectra of co-occurring organic tissue in the calcite skeleton of *Corallium* contained multiple organic S species including disulfide, thioether, sulfoxide, sulfone, and sulfate, while Mg-calcite sclerites from within the tissue contain thioether and sulfate (Tamenori et al., 2014; Perrin et al., 2017). The similarity between XANES spectra in multiple species of *Corallium* and *Coenites* sp., measured here (Fig. 3d, spectra 1-5), indicate that the biomineralization pathway of some extinct tabulate corals may be comparable to that of *Corallium*. Understanding the biomineralization pathway of fossil species is extremely important to interpreting geochemical signals from carbonates, especially CAS. Insights from these modern and ancient coral species indicate numerous sources of S (beyond seawater sulfate) that may be incorporated into carbonate skeletons during growth and/or recrystallization. Other OSCs are found within micrite and micritic envelopes seldom associated with specific fossil groups (e.g. Figs. 3a, 3c and 3d, XANES spectra 4 and 10) for the samples given here. This spatial independence makes it difficult to constrain early biomineralization pathways for all fossil groups. Additionally, upon traditional laboratory CAS extraction these compounds could be released, potentially contributing sulfate from multiple sources to the resulting bulk CAS signal and affecting geochemical proxies typically assumed to be sourced directly from seawater (e.g., [CAS] and $\delta^{34}\text{S}_{\text{CAS}}$).

All bioclast fragments in Fig. 3b (likely molluscs, corals and echinoderms, due to age, lack of preserved primary structure, and presence of syntaxial overgrowths) have a sulfate

abundance greater than that of the surrounding cement, but the abundance is variable between the bioclasts. Two different sulfate phases are observed between the moderate sulfate-containing bioclasts and the highest sulfate-containing bioclast (center, Fig. 3b); the energy of maximum intensity for the sulfate within the high-sulfate bioclast is at 2482.3 eV, which is downshifted from the sulfate contained within the other bioclasts in this region by 0.3 eV. This downshifting may correspond to differences in the lattice of the carbonate, i.e. the sulfate ion must change shape and lose symmetry in order to fit into the carbonate mineral phase (for primary aragonite or high-Mg calcite, Fernández-Díaz et al., 2010) resulting in a lower degeneracy of the sulfate orbital and therefore a slightly lower excitation energy relative to that for calcite (Cotton and Wilkinson, 1972). Although molluscs in this sample (predominantly gastropods and bivalves) may have made their shell structure out of aragonite, no aragonite is preserved. Echinoderms, however, generate their exoskeleton exclusively from high-Mg calcite (Flügel and Munnecke, 2010). Generally, high-Mg calcite will convert to low-Mg calcite over geologic time (due to diagenetic fluids removing Mg from the carbonate lattice), but the signal observed here indicates high-Mg calcite is preserved, likely in echinoderm fragments. The high sulfate abundance could reflect the amount of Mg in the calcite lattice, where increasing wt % Mg results in increased ability to incorporate sulfate, due to the smaller size of an Mg atom compared to Ca (Takano, 1985). The observation of sulfate abundance differences between high-Mg and low-Mg calcite bioclasts is an important finding as it indicates that the conversion from high- to low-Mg calcite on geologic timescales also results in the loss of primary sulfate.

As mentioned, sulfide is the dominant signal in all micrite components (interstitial, envelopes, clasts etc.). In all samples, numerous XANES spectra of sulfides within micrite show both sulfide and sulfate peaks (e.g. Fig. 3d locations 8 and 11 and Fig. 5e locations 2, 3 and 4),

where the intensity of the sulfide and sulfate peaks vary between locations within a given sample. This observation is strong evidence for the pervasive impact of oxidation of sulfide on the abundance of sulfate in micritic components. Oxidation of sulfide may occur at any stage after early diagenetic pyrite formation in the presence of an oxic fluid. These observations are in agreement with micro-drilled data from micrites that show low, yet variable, concentrations of sulfate with large isotopic variation from Anticosti Island samples (Present et al., 2015). These findings indicate that apparent CAS in micrite from ancient shallow-water carbonates may not be a faithful archive of original seawater sulfate and, instead, is likely a mixture of early and late diagenetic sources of sulfate, potentially including a high proportion of sulfate sourced from the oxidation of local pyrite. These results potentially call into question studies that target micrite as a more faithful recorder of CAS (e.g. Kampschulte and Strauss 2004; Wotte et al., 2012), but corroborate the need for multiple salt rinses to remove secondary sulfate phases prior to bulk CAS extraction (Wotte et al., 2012) and also highlight the importance of a petrographic context.

4.4 Correlating micron-scale observations with bulk data

The spatial variability of sulfide and sulfate abundance within a given sample, and between samples of different lithofacies, correlates with the changing proportions of carbonate components, shallow-water deposition, and early marine diagenesis. This correlation agrees with interpretations of bulk S abundance and isotope data from Anticosti Island and Gotland that are interpreted to reflect local, depositional-dependent processes (Jones and Fike, 2013; Rose et al., 2019). The bulk S-isotope datasets exhibit large samples-to-sample variability (up to 9‰ on Anticosti Island and 6 to 7‰ on Gotland; Jones and Fike, 2013 and Rose et al., 2019, respectively), characteristic of many bulk deep-time CAS datasets (Edwards et al., 2018;

Hurtgen et al., 2002; Kampschulte and Strauss, 2004; Osburn et al., 2015; Richardson et al., 2019; Ries et al., 2009; Thompson and Kah, 2012; Wotte et al., 2012b; Young et al., 2016). The carbonate strata from both localities record a paired $\delta^{13}\text{C}_{\text{carb}}-\delta^{13}\text{C}_{\text{org}}$ excursion, and where there is a coeval paired $\delta^{34}\text{S}_{\text{CAS}}-\delta^{34}\text{S}_{\text{pyr}}$ excursion on Gotland, a $\delta^{34}\text{S}_{\text{CAS}}$ excursion is absent on Anticosti Island. Commonly, a paired $\delta^{13}\text{C}_{\text{carb}}-\delta^{13}\text{C}_{\text{org}}$ and $\delta^{34}\text{S}_{\text{CAS}}-\delta^{34}\text{S}_{\text{pyr}}$ excursion in the rock record are explained by changes to the global sulfur cycle, such as increased pyrite burial. Time-correlative carbonates from within the same paleo-basin as Gotland do not show the same $\delta^{34}\text{S}_{\text{CAS}}-\delta^{34}\text{S}_{\text{pyr}}$ excursion (Richardson et al., 2019), indicating that the Gotland S-isotope data is locally controlled. Since the bulk sulfur isotopes from Anticosti Island and Gotland are not dominated by a global signal, we anticipate that variations in sulfate abundance in these samples is also not controlled by a changing sulfate concentrations at this time. This study helps explain the origin of the stratigraphic scatter in bulk $\delta^{34}\text{S}_{\text{CAS}}$ data from Anticosti Island and Gotland by demonstrating the impact that depositional environment has on the abundance of CAS and pyrite at the micron scale within each carbonate component, and between the same carbonate components under changing litho- and microfacies.

The identification of variable sulfate abundance within a single sample can be explained by processes during lithification, early marine diagenesis, and post-depositional alteration (Fig. 7). Initially, primary carbonate (as marine fauna) forms at the sediment water interface. During lithification, both blocky and drusy cement will form interstitial and pore-filling cements, and pyrite will form in the zone of sulfate reduction, provided a source of iron availability (Fig. 7, panel a). These cements will precipitate anywhere below the sediment-water interface, however drusy cements tend to have a higher precipitation rate, and, as such may form in the zone of sulfate reduction where carbonate precipitation is promoted. The difference in precipitation rate

between equant and drusy cements could result in increased incorporation of sulfate in drusy cement, or, equant cement could be forming below this region, where sulfate is less abundant or essentially absent as the result of progressive MSR. The difference in precipitation location between fossils and inorganic carbonate cements results in differences in the sulfate content of these components. This result is exemplified in the sulfate excitation map of a brachiopod and drusy cement from Gotland, where the brachiopod likely retains a primary seawater sulfate signature (Fig. 7, panel b, left hand side).

During early marine diagenesis (Fig. 7, panel b, right hand side), syntaxial cements may form when echinoderm fragments are within shallow depths of the sediment. Oxidation of pyrite may occur at any time after its formation, specifically in the presence of an oxic fluid and can occur syndepositionally (e.g., such as during early diagenetic reworking events that introduce oxygenated seawater deeper into the sediment; Fig. 7, panel b) as well as during late-stage diagenesis after lithification and burial. Any time after lithification, bioclasts and older cements may dissolve, generating new pores which may be infilled with drusy or equant cement at any time, ultimately forming from a different source fluid (Fig. 7, panel b, right hand side). This model has variable and changing abundance and $\delta^{34}\text{S}$ of SO_4^{2-} and H_2S within the sediment, due to the fractionation occurring during MSR and relative depth in the sediment (Fike et al., 2015). As MSR progresses in the sediment, $\delta^{34}\text{S}_{\text{SO}_4}$ moves towards heavier values as the lighter isotope is consumed preferentially during MSR. As such, $\delta^{34}\text{S}_{\text{H}_2\text{S}}$ follows this trend towards heavier values (offset by the microbial fractionation) as the source pool continues to become enriched in ^{34}S . In shallow-water environments where sedimentation rate is high, and labile organic carbon and Fe are available, S-isotopes may evolve under more closed-system conditions (Claypool, 2004) as described above. The frequency of sediment reworking events in shallow-water

environments introduces new sulfate into the sediment, essentially resetting the distillation process of isotopes. These processes should be reflected in both $\delta^{34}\text{S}_{\text{CAS}}$ and $\delta^{34}\text{S}_{\text{pyr}}$ at the bulk (Richardson et al., 2019) and micron scales. Ultimately this model for different CAS content of individual carbonate components within a given sample may contribute to the elevated sample-to-sample variability in bulk-rock $\delta^{34}\text{S}_{\text{CAS}}$ datasets throughout Earth history (e.g., Kampschulte and Strauss 2004; Jones and Fike 2013; Osburn et al., 2015), where changes in this variability in a stratigraphic section may relate to changes in the relative proportions of the different cements or other carbonate components resulting from varying depositional conditions. Future work characterizing the S-isotopic composition of each component is imperative to understanding the degree to which marine diagenesis is the cause of the inherent variability in all bulk $\delta^{34}\text{S}_{\text{CAS}}$ datasets.

As mentioned, we expect that disseminated sulfides are likely to be a major component in all forms of micrite present in carbonate sections throughout Earth history. It has been shown that laboratory oxidation of granular sulfide ($< 300 \mu\text{m}$) during acid extraction can appreciably affect bulk CAS at sulfide abundances greater than 1 weight % (Marenco et al., 2008). In studied carbonate sections however, pyrite generally occurs at less than 1 weight % (e.g. Jones and Fike 2013; Richardson et al., 2019; Rose et al., 2019) and thus it is assumed that pyrite oxidation during laboratory extractions does not greatly affect bulk CAS measurements, especially in the absence of a correlation between, wt. % pyrite and CAS abundance, as well as CAS abundance and $\delta^{34}\text{S}_{\text{CAS}}$. However, this does not preclude an impact on CAS from sulfides that have already undergone (partial) oxidation during post-depositional diagenesis. Such partial oxidation of pyrites has been demonstrated to exist in all samples containing micrite here using XANES spectroscopy (Fig. 5e). This sulfate (originally sourced from pyrite) may be sorbed onto the

micrite surface and may be incorporated as CAS during an extraction, ultimately driving the isotopic value of the sample towards lighter values. As such, it is important that CAS extraction protocols incorporate multiple brine rinses to remove any sulfate that is not lattice bound (Wotte et al., 2012)

The extremely low abundance of preserved OSCs in corals and in micrite observed here are not anticipated to affect bulk CAS measurements. However, the role of OSCs during biotic carbonate growth is unknown; as such, CAS in well-preserved fossils could reflect a complex mixture of inorganic and organic S sources, resulting in a CAS signal distinct from that of coeval seawater. A majority of fossils preserved in ancient carbonates are commonly recrystallized or micritized, and sulfate abundance is variable. Thus, we anticipate that, unless the fossils preserve original mineralogy and structure, the sulfate signal is unlikely to be completely primary. Differences in sulfate abundance between fossil fragments may record the relative difference in primary CAS, as it is assumed all fossils of a given group within a petrographic thin section should be (approximately) affected equally by diagenesis. Since the primary CAS content of extinct fossil groups is largely unknown, it is difficult to infer the source of diagenetic fluids that they may have been exposed to. Moving forward, it will be important to gain a greater understanding of the source of sulfate in modern biomineralizers from abundance and isotope studies of single species. This knowledge will provide a platform to assess sulfate variability within a given species (and perhaps genus), and how this may result in variable sulfate abundance after diagenesis. Broad-scale meteoric diagenesis can be precluded from both localities due to the variability of sulfate in a given sample, heterogeneity that would be lost during wholesale meteoric diagenesis. Thus, we anticipate that marine or evolved marine waters are the dominant source of diagenetic sulfate in fossils observed in the present study. The

addition of isotope data to the regions mapped in this study will provide a more robust understanding of primary and secondary signals, and the source of secondary signals. Further, component-specific isotope analyses will aid our understanding and interpretation of highly variable bulk $\delta^{34}\text{S}_{\text{CAS}}$ datasets.

5.0 Conclusions

High resolution μ -XRF imaging and XANES spectroscopy at the S K-edge in ancient carbonates reveals the presence and variable abundance of multiple S-species (predominantly sulfide and sulfate) in a range of lithofacies from shallow water marine carbonates. Investigation of fossils, cement, micrite, and abiotic grains across multiple lithofacies indicates that shallow-water depositional environments and early marine diagenesis are strong controls on the abundance and spatial variability of S-species, agreeing with recent studies on bulk S-isotopes that suggest depositional environment (e.g. sediment reworking, iron availability, and sedimentation rate) contributes to S-isotope variability. Well-preserved brachiopods and bryozoans have the highest sulfate abundance of all fossil groups studied, indicating these components might serve as two potential archives for robust CAS measurements. The identification of multiple OSCs in fossil tabulate corals, similar to OSCs inferred to be present in modern, deep-water corals, points towards a similar biomineralization pathway in extinct fossil groups. Elucidating such biomineralization pathways will aid our understanding of the source(s) of CAS in ancient carbonates and future interpretations of other geochemical proxies obtained from extinct fossil groups. In this sample set, cements contain inorganic sulfate, where variability in abundance reflects changes in pore fluid composition and precipitation rates during early marine diagenesis. We anticipate that such variation in sulfate abundance is not limited to the samples here and will

occur in most other cements forming at various depths with carbonate sediment. Inorganic sulfate in bioclast fragments is observed to have two excitation energies ~ 0.3 eV apart. This shifting of the sulfate excitation energy reflects changes in the carbonate mineralogy (low- vs. high-Mg calcite). Sulfides, and sulfate sourced from the oxidation of sulfides, is dominant in micritic components and facies. The high abundance of sulfide reflects the availability of Fe and labile organic matter (thereby promoting MSR) in fine-grained sediments from shallow-water carbonate environments, with the oxidation of sulfide occurring progressively over time in contact with oxic diagenetic fluids. Together, these observations suggest that CAS sourced from shallow-water micrite components in carbonate rocks is not inherently a reliable recorder of ancient seawater sulfate during deposition and highlights the μ -scale sulfate variability that bulk CAS records are masking. Future studies aiming to reconstruct the operation of the sulfur cycle during key intervals of Earth history should exercise caution when homogenizing shallow-water carbonates that mix variable abundances of different carbonate components that formed throughout lithification and early marine diagenesis, particularly shallow-water facies that are micrite dominated. We recommend that studies target unaltered fossil fragments that retain primary mineralogy and fabric, or deep-water carbonate facies where porewater is more connected to the overlying seawater, reducing any signal from isotope distillation during early marine diagenesis.

Acknowledgements

We thank R. Nickerson and C. Roach for help and discussion during beam time and A. Munnecke for useful comments on carbonate petrography. We would also like to thank M. Böttcher and two anonymous reviewers for helping to improve this manuscript. Acknowledgment is made to the donors of the American Chemical Society Petroleum Research Fund (#57548-ND2) for partial support of this research. Use of the Stanford Synchrotron Radiation Lightsource, SLAC National Accelerator Laboratory, is supported by the U.S. Department of Energy, Office of Science, Office of Basic Energy Sciences under Contract No.

DE-AC02-76SF00515. The SSRL Structural Molecular Biology Program is supported by the DOE Office of Biological and Environmental Research, and by the National Institutes of Health, National Institute of General Medical Sciences (including P41GM103393). The contents of this publication are solely the responsibility of the authors and do not necessarily represent the official views of NIGMS or NIH. This research used resources of the Advanced Photon Source, a U.S. Department of Energy (DOE) Office of Science User Facility operated for the DOE Office of Science by Argonne National Laboratory under Contract No. DE-AC02-06CH11357.

References

- Aller, R.C., Madrid, V., Chistoserdov, A., Aller, J.Y., Heilbrun, C., 2010. Unsteady diagenetic processes and sulfur biogeochemistry in tropical deltaic muds: Implications for oceanic isotope cycles and the sedimentary record. *Geochim. Cosmochim. Acta* 74, 4671–4692. <https://doi.org/10.1016/j.gca.2010.05.008>
- Almkvist, G., Boye, K., Persson, I., 2010. K-edge XANES analysis of sulfur compounds: An investigation of the relative intensities using internal calibration. *J. Synchrotron Radiat.* 17, 683–688. <https://doi.org/10.1107/S0909049510022946>
- Baumgartner, L.K., Reid, R.P., Dupraz, C., Decho, A.W., Buckley, D.H., Spear, J.R., Przekop, K.M., Visscher, P.T., 2006. Sulfate reducing bacteria in microbial mats: Changing paradigms, new discoveries. *Sediment. Geol.* 185, 131–145. <https://doi.org/10.1016/J.SEDGEO.2005.12.008>
- Berner, R.A., 2001. Modeling atmospheric O₂ over Phanerozoic time. *Geochim. Cosmochim. Acta* 65, 685–694. [https://doi.org/10.1016/S0016-7037\(00\)00572-X](https://doi.org/10.1016/S0016-7037(00)00572-X)
- Berner, R.A., Raiswell, R., 1983. Burial of organic carbon and pyrite sulfur in sediments over phanerozoic time: a new theory. *Geochim. Cosmochim. Acta* 47, 855–862. [https://doi.org/10.1016/0016-7037\(83\)90151-5](https://doi.org/10.1016/0016-7037(83)90151-5)
- Berner, R.A., Scott, M.R., Thomlinson, C., 1970. Carbonate alkalinity in the pore waters of anoxic marine sediments. *Limnol. Oceanogr.* 15, 544–549.

<https://doi.org/10.4319/lo.1970.15.4.0544>

Brand, U., Veizer, J., 1980. Chemical Diagenesis of a Multicomponent Carbonate System--1:

Trace Elements. *SEPM J. Sediment. Res.* Vol. 50, 1219–1236.

<https://doi.org/10.1306/212F7BB7-2B24-11D7-8648000102C1865D>

Burdett, J.W., Arthur, M.A., Richardson, M., 1989. A Neogene seawater sulfur isotope age curve from calcareous pelagic microfossils. *Earth Planet. Sci. Lett.* 94, 189–198.

[https://doi.org/10.1016/0012-821X\(89\)90138-6](https://doi.org/10.1016/0012-821X(89)90138-6)

Busenberg, E., Plummer, N.L., 1985. Kinetic and thermodynamic factors controlling the distribution of SO_3^{2-} and Na^+ in calcites and selected aragonites. *Geochim. Cosmochim. Acta* 49, 713–725. [https://doi.org/10.1016/0016-7037\(85\)90166-8](https://doi.org/10.1016/0016-7037(85)90166-8)

Canfield, D.E., 2004. The evolution of the Earth surface sulfur reservoir. *Am. J. Sci.* 304, 839–861. <https://doi.org/10.2475/ajs.304.10.839>

Christ, N., Immenhauser, A., Wood, R.A., Darwich, K., Niedermayr, A., 2015. Petrography and environmental controls on the formation of Phanerozoic marine carbonate hardgrounds. *Earth-Science Rev.* 151, 176–226. <https://doi.org/10.1016/J.EARSCIREV.2015.10.002>

Claypool, G.E., 2004. Ventilation of marine sediments indicated by depth profiles of pore water sulfate and $\delta^{34}\text{S}$. *Geochemical Soc. Spec. Publ.* 9, 59–65. [https://doi.org/10.1016/S1873-9881\(04\)80007-5](https://doi.org/10.1016/S1873-9881(04)80007-5)

Cocks, L.R.M., Torsvik, T.H., 2002. Earth geography from 500 to 400 million years ago: a faunal and palaeomagnetic review. *J. Geol. Soc. London.* 159, 631–644.

<https://doi.org/10.1144/0016-764901-118>

Cotton, F.A., Wilkinson, G., 1972. *Advanced Inorganic Chemistry*, 3rd ed. Wiley.

Crowe, S.A., Paris, G., Katsev, S., Jones, C., Kim, S.-T., Zerkle, A.L., Nomosatryo, S., Fowle,

- D.A., Adkins, J.F., Sessions, A.L., Farquhar, J., Canfield, D.E., 2014. Sulfate was a trace constituent of Archean seawater. *Science* 346, 735–9.
<https://doi.org/10.1126/science.1258966>
- Cuif, J.-P., Dauphin, Y., Doucet, J., Salomé, M., Susini, J., 2003. XANES mapping of organic sulfate in three scleractinian coral skeletons. *Geochim. Cosmochim. Acta* 67, 75–83.
[https://doi.org/10.1016/S0016-7037\(02\)01041-4](https://doi.org/10.1016/S0016-7037(02)01041-4)
- Cusack, M., Dauphin, Y., Cuif, J.-P., Salomé, M., Freer, A., Yin, H., 2008. Micro-XANES mapping of sulphur and its association with magnesium and phosphorus in the shell of the brachiopod, *Terebratulina retusa*. *Chem. Geol.* 253, 172–179.
<https://doi.org/10.1016/J.CHEMGEO.2008.05.007>
- Dauphin, Y., Cuif, J.-P., Doucet, J., Salomé, M., Susini, J., Terry Willams, C., 2003. In situ chemical speciation of sulfur in calcitic biominerals and the simple prism concept. *J. Struct. Biol.* 142, 272–280. [https://doi.org/10.1016/S1047-8477\(03\)00054-6](https://doi.org/10.1016/S1047-8477(03)00054-6)
- Desrochers, A., Farley, C., Achab, A., Asselin, E., Riva, J.F., 2010. A far-field record of the end Ordovician glaciation: The Ellis Bay Formation, Anticosti Island, Eastern Canada. *Palaeogeogr. Palaeoclimatol. Palaeoecol.* 296, 248–263.
<https://doi.org/10.1016/j.palaeo.2010.02.017>
- Edwards, C.T., Fike, D.A., Saltzman, M.R., Lu, W., Lu, Z., 2018. Evidence for local and global redox conditions at an Early Ordovician (Tremadocian) mass extinction. *Earth Planet. Sci. Lett.* 481, 125–135. <https://doi.org/10.1016/J.EPSL.2017.10.002>
- Ernst, A., Munnecke, A., 2009. A Hirnantian (latest Ordovician) reefal bryozoan fauna from Anticosti Island, eastern Canada: taxonomy and chemostratigraphy. *Can. J. Earth Sci.* 46, 207–229. <https://doi.org/10.1139/E09-017>

- Fernández-Díaz, L., Fernández-González, Á., Prieto, M., 2010. The role of sulfate groups in controlling CaCO₃ polymorphism. *Geochim. Cosmochim. Acta* 74, 6064–6076.
<https://doi.org/10.1016/J.GCA.2010.08.010>
- Fichtner, V., Strauss, H., Immenhauser, A., Buhl, D., Neuser, R.D., Niedermayr, A., 2017. Diagenesis of carbonate associated sulfate. *Chem. Geol.* 463, 61–75.
<https://doi.org/10.1016/J.CHEMGEO.2017.05.008>
- Fike, D.A., Bradley, A.S., Rose, C. V., 2015. Rethinking the Ancient Sulfur Cycle. *Annu. Rev. Earth Planet. Sci.* 43, 593–622. <https://doi.org/10.1146/annurev-earth-060313-054802>
- Fike, D.A., Grotzinger, J.P., 2008. A paired sulfate–pyrite $\delta^{34}\text{S}$ approach to understanding the evolution of the Ediacaran–Cambrian sulfur cycle. *Geochim. Cosmochim. Acta* 72, 2636–2648. <https://doi.org/10.1016/j.gca.2008.03.021>
- Flügel, E., Munnecke, A., 2010. *Microfacies of carbonate rocks : analysis, interpretation and application*. Springer.
- Folk, R.L., 1965. *Some Aspects of Recrystallization in Ancient Limestones*.
- Frisia, S., Borsato, A., Fairchild, I.J., Susini, J., 2005. Variations in atmospheric sulphate recorded in stalagmites by synchrotron micro-XRF and XANES analyses. *Earth Planet. Sci. Lett.* 235, 729–740. <https://doi.org/10.1016/J.EPSL.2005.03.026>
- Gill, B.C., Lyons, T.W., Frank, T.D., 2008. Behavior of carbonate-associated sulfate during meteoric diagenesis and implications for the sulfur isotope paleoproxy. *Geochim. Cosmochim. Acta* 72, 4699–4711. <https://doi.org/10.1016/J.GCA.2008.07.001>
- Gill, B.C., Lyons, T.W., Jenkyns, H.C., 2011. A global perturbation to the sulfur cycle during the Toarcian Oceanic Anoxic Event. *Earth Planet. Sci. Lett.* 312, 484–496.
<https://doi.org/10.1016/J.EPSL.2011.10.030>

- Gill, B.C., Lyons, T.W., Saltzman, M.R., 2007. Parallel, high-resolution carbon and sulfur isotope records of the evolving Paleozoic marine sulfur reservoir. *Palaeogeogr. Palaeoclimatol. Palaeoecol.* 256, 156–173. <https://doi.org/10.1016/J.PALAEO.2007.02.030>
- Hedman, B., Frank, P., Penner-Hahn, J.E., Roe, A.L., Hodgson, K.O., Carlson, R.M.K., Brown, G., Cerino, J., Hettel, R., Troxel, T., Winick, H., Yang, J., 1986. Sulfur K-edge X-ray absorption studies using the 54-pole wiggler at SSRL in undulator mode. *Nucl. Instruments Methods Phys. Res. Sect. A Accel. Spectrometers, Detect. Assoc. Equip.* 246, 797–800. [https://doi.org/10.1016/0168-9002\(86\)90196-8](https://doi.org/10.1016/0168-9002(86)90196-8)
- Hurtgen, M.T., Arthur, M.A., Suits, N.S., Kaufman, A.J., 2002. The sulfur isotopic composition of Neoproterozoic seawater sulfate: implications for a snowball Earth? *Earth Planet. Sci. Lett.* 203, 413–429. [https://doi.org/10.1016/S0012-821X\(02\)00804-X](https://doi.org/10.1016/S0012-821X(02)00804-X)
- Hurtgen, M.T., Halverson, G.P., Arthur, M.A., Hoffman, P.F., 2006. Sulfur cycling in the aftermath of a 635-Ma snowball glaciation: Evidence for a syn-glacial sulfidic deep ocean. *Earth Planet. Sci. Lett.* 245, 551–570. <https://doi.org/10.1016/j.epsl.2006.03.026>
- Hurtgen, M.T., Pruss, S.B., Knoll, A.H., 2009. Evaluating the relationship between the carbon and sulfur cycles in the later Cambrian ocean: An example from the Port au Port Group, western Newfoundland, Canada. *Earth Planet. Sci. Lett.* 281, 288–297. <https://doi.org/10.1016/J.EPSL.2009.02.033>
- Jarochowska, E., Munnecke, A., 2014. The Paleozoic problematica *Wetheredella* and *Allonema* are two aspects of the same organism. *Facies* 60, 651–662. <https://doi.org/10.1007/s10347-014-0399-z>
- Jeppsson, L., 1983. Silurian conodont faunas from Gotland. *Foss. Strat.* 15, 121–144.
- Jones, D.S., Fike, D.A., 2013. Dynamic sulfur and carbon cycling through the end-Ordovician

extinction revealed by paired sulfate–pyrite $\delta^{34}\text{S}$. *Earth Planet. Sci. Lett.* 363, 144–155.

<https://doi.org/10.1016/j.epsl.2012.12.015>

Jones, D.S., Fike, D.A., Finnegan, S., Fischer, W.W., Schrag, D.P., McCay, D., 2011. Terminal Ordovician carbon isotope stratigraphy and glacioeustatic sea-level change across Anticosti Island (Québec, Canada). *Bull. Geol. Soc. Am.* 123, 1645–1664.

<https://doi.org/10.1130/B30323.1>

Kampschulte, A., Bruckschen, P., Strauss, H., 2001. The sulphur isotopic composition of trace sulphates in Carboniferous brachiopods: implications for coeval seawater, correlation with other geochemical cycles and isotope stratigraphy. *Chem. Geol.* 175, 149–173.

[https://doi.org/10.1016/S0009-2541\(00\)00367-3](https://doi.org/10.1016/S0009-2541(00)00367-3)

Kampschulte, A., Strauss, H., 2004. The sulfur isotopic evolution of Phanerozoic seawater based on the analysis of structurally substituted sulfate in carbonates. *Chem. Geol.* 204, 255–286.

<https://doi.org/10.1016/J.CHEMGEO.2003.11.013>

Kile, D., Eberl, D., Hoch, A., Reddy, M., 2000. An assessment of calcite crystal growth mechanisms based on crystal size distributions. *Geochim. Cosmochim. Acta* 64, 2937–2950. [https://doi.org/10.1016/S0016-7037\(00\)00394-X](https://doi.org/10.1016/S0016-7037(00)00394-X)

Kozik, N.P., Young, S.A., Bowman, C.N., Saltzman, M.R., Them, T.R., 2019. Middle–Upper Ordovician (Darriwilian–Sandbian) paired carbon and sulfur isotope stratigraphy from the Appalachian Basin, USA: Implications for dynamic redox conditions spanning the peak of the Great Ordovician Biodiversification Event. *Palaeogeogr. Palaeoclimatol. Palaeoecol.* 520, 188–202. <https://doi.org/10.1016/j.palaeo.2019.01.032>

Langdon, C., Takahashi, T., Sweeney, C., Chipman, D., Goddard, J., Marubini, F., Aceves, H., Barnett, H., Atkinson, M.J., 2000. Effect of calcium carbonate saturation state on the

- calcification rate of an experimental coral reef. *Global Biogeochem. Cycles* 14, 639–654.
<https://doi.org/10.1029/1999GB001195>
- Leavitt, W.D., Halevy, I., Bradley, A.S., Johnston, D.T., 2013. Influence of sulfate reduction rates on the Phanerozoic sulfur isotope record. *Proc. Natl. Acad. Sci. U. S. A.* 110, 11244–9. <https://doi.org/10.1073/pnas.1218874110>
- Lehnert, O., Männik, P., Joachimski, M.M., Calner, M., Frýda, J., 2010. Palaeoclimate perturbations before the Sheinwoodian glaciation: A trigger for extinctions during the ‘Ireviken Event.’ *Palaeogeogr. Palaeoclimatol. Palaeoecol.* 296, 320–331.
<https://doi.org/10.1016/j.palaeo.2010.01.009>
- Long, D.G.F., Copper, P., 1987. Stratigraphy of the Upper Ordovician upper Vaureal and Ellis Bay formations, eastern Anticosti Island, Quebec. *Can. J. Earth Sci.* 24, 1807–1820.
<https://doi.org/10.1139/e87-172>
- Lowenstam, H.A., 1961. Mineralogy, O^{18}/O^{16} Ratios, and Strontium and Magnesium Contents of Recent and Fossil Brachiopods and Their Bearing on the History of the Oceans. *J. Geol.* 69, 241–260. <https://doi.org/10.1086/626740>
- Marenco, P.J., Corsetti, F.A., Hammond, D.E., Kaufman, A.J., Bottjer, D.J., 2008. Oxidation of pyrite during extraction of carbonate associated sulfate. *Chem. Geol.* 247, 124–132.
<https://doi.org/10.1016/j.chemgeo.2007.10.006>
- Mayhew, L.E., Webb, S.M., Templeton, A.S., 2011. Microscale Imaging and Identification of Fe Speciation and Distribution during Fluid–Mineral Reactions under Highly Reducing Conditions. *Environ. Sci. Technol.* 45, 4468–4474. <https://doi.org/10.1021/es104292n>
- Munnecke, A., Calner, M., Harper, D.A.T., Servais, T., 2010. Ordovician and Silurian sea–water chemistry, sea level, and climate: A synopsis. *Palaeogeogr. Palaeoclimatol. Palaeoecol.* 296,

389–413. <https://doi.org/10.1016/j.palaeo.2010.08.001>

- Munnecke, A., Samtleben, C., Bickert, T., 2003. The Ireviken Event in the lower Silurian of Gotland, Sweden – relation to similar Palaeozoic and Proterozoic events. *Palaeogeogr. Palaeoclimatol. Palaeoecol.* 195, 99–124. [https://doi.org/10.1016/S0031-0182\(03\)00304-3](https://doi.org/10.1016/S0031-0182(03)00304-3)
- Newville, M., 2013. Larch: An Analysis Package for XAFS And Related Spectroscopies, *Journal of Physics. J. Phys. Conf. Ser.* 430.
- Osburn, M.R., Owens, J., Bergmann, K.D., Lyons, T.W., Grotzinger, J.P., 2015. Dynamic changes in sulfate sulfur isotopes preceding the Ediacaran Shuram Excursion. *Geochim. Cosmochim. Acta* 170, 204–224. <https://doi.org/10.1016/J.GCA.2015.07.039>
- Paris, G., Adkins, J.F., Sessions, A.L., Webb, S.M., Fischer, W.W., 2014. Neoproterozoic carbonate-associated sulfate records positive $\Delta^{33}\text{S}$ anomalies. *Science* 346, 739–41. <https://doi.org/10.1126/science.1258211>
- Pasquier, V., Sansjofre, P., Rabineau, M., Revillon, S., Houghton, J., Fike, D.A., 2017. Pyrite sulfur isotopes reveal glacial–interglacial environmental changes. *Proc. Natl. Acad. Sci.* 114, 5941–5945. <https://doi.org/10.1073/pnas.1618245114>
- Perrin, J., Rivard, C., Vielzeuf, D., Laporte, D., Fonquernie, C., Ricolleau, A., Cotte, M., Floquet, N., 2017. The coordination of sulfur in synthetic and biogenic Mg calcites: The red coral case. *Geochim. Cosmochim. Acta* 197, 226–244. <https://doi.org/10.1016/J.GCA.2016.10.017>
- Pinet, N., Lavoie, D., 2007. The Offshore Part of the Anticosti Basin: A Major Gap in the Understanding of Early to Middle Paleozoic Basins of Eastern Canada in a Promising Hydrocarbon Setting, *Convention Extended Abstracts: Calgary, Canadian Society of Petroleum and Geology.*

- Present, T.M., Paris, G., Burke, A., Fischer, W.W., Adkins, J.F., 2015. Large Carbonate Associated Sulfate isotopic variability between brachiopods, micrite, and other sedimentary components in Late Ordovician strata. *Earth Planet. Sci. Lett.* 432, 187–198.
<https://doi.org/10.1016/J.EPSL.2015.10.005>
- Rennie, V.C.F., Paris, G., Sessions, A.L., Abramovich, S., Turchyn, A. V., Adkins, J.F., 2018. Cenozoic record of $\delta^{34}\text{S}$ in foraminiferal calcite implies an early Eocene shift to deep-ocean sulfide burial. *Nat. Geosci.* 1. <https://doi.org/10.1038/s41561-018-0200-y>
- Rennie, V.C.F., Turchyn, A. V., 2014. The preservation of $\delta^{\text{SSO}434}$ and $\delta^{\text{OSO}418}$ in carbonate-associated sulfate during marine diagenesis: A 25 Myr test case using marine sediments. *Earth Planet. Sci. Lett.* 395, 13–23. <https://doi.org/10.1016/J.EPSL.2014.03.025>
- Riccardi, A.L., Arthur, M.A., Kump, L.R., 2006. Sulfur isotopic evidence for chemocline upward excursions during the end-Permian mass extinction. *Geochim. Cosmochim. Acta* 70, 5740–5752. <https://doi.org/10.1016/J.GCA.2006.08.005>
- Richardson, J.A., Keating, C., Lepland, A., Hints, O., Bradley, A.S., Fike, D.A., 2019. Silurian records of carbon and sulfur cycling from Estonia: The importance of depositional environment on isotopic trends. *Earth Planet. Sci. Lett.* 512, 71–82.
<https://doi.org/10.1016/J.EPSL.2019.01.055>
- Ries, J.B., Fike, D.A., Pratt, L.M., Lyons, T.W., Grotzinger, J.P., 2009. Superheavy pyrite ($^{34}\text{S}_{\text{pyr}}$ > $^{34}\text{S}_{\text{CAS}}$) in the terminal Proterozoic Nama Group, southern Namibia: A consequence of low seawater sulfate at the dawn of animal life. *Geology* 37, 743–746.
<https://doi.org/10.1130/G25775A.1>
- Rose, C. V., Fischer, W.W., Finnegan, S., Fike, D.A., 2019. Records of carbon and sulfur cycling during the Silurian Ireviken Event in Gotland, Sweden. *Geochim. Cosmochim. Acta*

- 246, 299–316. <https://doi.org/10.1016/J.GCA.2018.11.030>
- Rose, C. V., Webb, S.M., Newville, M., Lanzirrotti, A., Richardson, J.A., Tosca, N.J., Catalano, J.G., Bradley, A.S., Fike, D.A., n.d. Insights into Past Ocean Proxies from Micron-scale Mapping of Sulfur Species in Carbonates.
- Scholle, P.A., Ulmer-Scholle, D.S., 2003. A Color Guide to the Petrography of Carbonate Rocks: Grains, textures, porosity, diagenesis, Aapg Memoir. <https://doi.org/10.1306/m77973>
- Sim, M.S., Bosak, T., Ono, S., 2011. Large sulfur isotope fractionation does not require disproportionation. *Science* 333, 74–7. <https://doi.org/10.1126/science.1205103>
- Smith, A.M., Key, M.M., Gordon, D.P., 2006. Skeletal mineralogy of bryozoans: Taxonomic and temporal patterns. *Earth-Science Rev.* 78, 287–306. <https://doi.org/10.1016/J.EARSCIREV.2006.06.001>
- Staudt, W.J., Reeder, R.J., Schoonen, M.A.A., 1994. Surface structural controls on compositional zoning of SO_2-4 and SeO_2-4 in synthetic calcite single crystals. *Geochim. Cosmochim. Acta* 58, 2087–2098. [https://doi.org/10.1016/0016-7037\(94\)90287-9](https://doi.org/10.1016/0016-7037(94)90287-9)
- Staudt, W.J., Schoonen, M.A.A., 1995. Sulfate Incorporation into Sedimentary Carbonates. pp. 332–345. <https://doi.org/10.1021/bk-1995-0612.ch018>
- Strauss, H., 1997. The isotopic composition of sedimentary sulfur through time. *Palaeogeogr. Palaeoclimatol. Palaeoecol.* 132, 97–118. [https://doi.org/10.1016/S0031-0182\(97\)00067-9](https://doi.org/10.1016/S0031-0182(97)00067-9)
- Takano, B., 1985. Geochemical implications of sulfate in sedimentary carbonates. *Chem. Geol.* 49, 393–403. [https://doi.org/10.1016/0009-2541\(85\)90001-4](https://doi.org/10.1016/0009-2541(85)90001-4)
- Tamenori, Y., Yoshimura, T., Luan, N.T., Hasegawa, H., Suzuki, A., Kawahata, H., Iwasaki, N., 2014. Identification of the chemical form of sulfur compounds in the Japanese pink coral (*Corallium elatius*) skeleton using μ -XRF/XAS speciation mapping. *J. Struct. Biol.* 186,

214–223. <https://doi.org/10.1016/J.JSB.2014.04.001>

Thompson, C.K., Kah, L.C., 2012. Sulfur isotope evidence for widespread euxinia and a fluctuating oxycline in Early to Middle Ordovician greenhouse oceans. *Palaeogeogr. Palaeoclimatol. Palaeoecol.* 313–314, 189–214.

<https://doi.org/10.1016/J.PALAEO.2011.10.020>

Toth, D.J., Lerman, A., 1977. Organic matter reactivity and sedimentation rates in the ocean. *Am. J. Sci.* 277, 465–485. <https://doi.org/10.2475/ajs.277.4.465>

Turchyn, A. V., Schrag, D.P., Coccioni, R., Montanari, A., 2009. Stable isotope analysis of the Cretaceous sulfur cycle. *Earth Planet. Sci. Lett.* 285, 115–123.

<https://doi.org/10.1016/J.EPSL.2009.06.002>

Walker, K.R., Jernigan, D.G., Weber, L.J., 1990. Petrographic criteria for the recognition of marine, syntaxial overgrowths, and their distribution in geologic time. *Carbonates and Evaporites* 5, 141–152. <https://doi.org/10.1007/BF03174845>

Webb, S.M., 2005. SIXPack a Graphical User Interface for XAS Analysis Using IFEFFIT. *Phys. Scr.* 2005, 1011. <https://doi.org/10.1238/Physica.Topical.115a01011>

Webb, S.M., McNulty, I., Eyberger, C., Lai, B., 2011. The MicroAnalysis Toolkit: X-ray Fluorescence Image Processing Software, in: *AIP Conference Proceedings*. American Institute of Physics, pp. 196–199. <https://doi.org/10.1063/1.3625338>

Wilke, M., Jugo, P.J., Klimm, K., Susini, J., Botcharnikov, R., Kohn, S.C., Janousch, M., 2008. The origin of S⁴⁺ detected in silicate glasses by XANES. *Am. Mineral.* 93, 235–240. <https://doi.org/10.2138/am.2008.2765>

Wotte, T., Shields-Zhou, G.A., Strauss, H., 2012a. Carbonate-associated sulfate: Experimental comparisons of common extraction methods and recommendations toward a standard

analytical protocol. *Chem. Geol.* 326–327, 132–144.

<https://doi.org/10.1016/J.CHEMGEO.2012.07.020>

Wotte, T., Strauss, H., Fugmann, A., Garbe-Schönberg, D., 2012b. Paired $\delta^{34}\text{S}$ data from carbonate-associated sulfate and chromium-reducible sulfur across the traditional Lower–Middle Cambrian boundary of W-Gondwana. *Geochim. Cosmochim. Acta* 85, 228–253.
<https://doi.org/10.1016/J.GCA.2012.02.013>

Yoshimura, T., Tamenori, Y., Suzuki, A., Nakashima, R., Iwasaki, N., Hasegawa, H., Kawahata, H., 2013. Element profile and chemical environment of sulfur in a giant clam shell: Insights from μ -XRF and X-ray absorption near-edge structure. *Chem. Geol.* 352, 170–175.
<https://doi.org/10.1016/J.CHEMGEO.2013.05.035>

Young, S.A., Gill, B.C., Edwards, C.T., Leslie, S.A., 2016. Middle–Late Ordovician (Darriwilian–Sandbian) decoupling of global sulfur and carbon cycles: Isotopic evidence from eastern and southern Laurentia. *Palaeogeogr. Palaeoclimatol. Palaeoecol.* 458, 118–132. <https://doi.org/10.1016/J.PALAEO.2015.09.040>

Fig. 1 – a.) Paleogeographic reconstruction of Laurentia and Baltica at the Ordovician-Silurian boundary (~ 440 Ma) including locations of Anticosti Island and Gotland. Modified from Cocks and Torsvik, (2002) b.) geologic map of Anticosti Island with sample locations annotated. A generalized stratigraphic section is shown on the left (modified from Jones et al., 2011 and Jones and Fike 2013) and c.) geologic map of Gotland with sample locations annotated including a generalized stratigraphic section on the left (modified from Rose et al., 2019).

Fig. 2 – Standard XANES of common sulfur species in the S K-edge region obtained at BL 13-IDE. Pyrite standard from Konecke et al. (2017) and chondroitin sulfate (ester) standard from the ESRF ID-21 S XANES spectra database (Cuif et al., 2003).

Fig. 3 – Photomicrographs showing a variety of fossils, fossil fragments and grains with corresponding sulfate energy map (sulfide subtracted) on the right. A = *Allonema*, C = *Coenites sp.*, M = micrite infilling, ME = micrite envelope, SO = syntaxial overgrowth, MB = micritized bioclast, RU = Rugose, RC = recrystallized centre. Map colors correspond to abundance where black is minimum and white is maximum abundance (applies to all maps) a.) *Coenites sp.*, with *Allonema* (inset) from a coral grainstone from the Upper Visby Formation, Gotland b.) Fossiliferous grainstone from an oncolite platform, Lousy Cove Member, Anticosti Island c.) another region of sample in b. where the high sulfate bioclasts are similar to the high sulfate bioclast in b, and d.) XANES of locations numbered in a-c with important peak energies annotated.

Fig. 4 - Photomicrographs (left) showing a variety of cement fabrics as interstitial cement and diagenetic features with corresponding sulfide (centre) and sulfate (right; sulfide removed) energy maps for each panel. BL = blocky, DR = drusy, SO = syntaxial overgrowth, B = brachiopod and BRY = bryozoan a.) petrographic thin section image of intra-hermal sample, Lousy Cove Member, Anticosti Island, b.) bioclastic grainstone from the Lower Tofta Formation, Gotland, c.) poorly washed fossiliferous grainstone from the Upper Visby Formation, Gotland, d.) brachiopodal grainstone from Gotland.

Fig. 5 – a.) Photomicrograph of a crinoidal wackestone Lousy Cove Member, Anticosti Island. b.) sulfide energy map (2472.0 eV) of (a); numbers depict representative XANES spectra. c) map of sulfate energy (2482.3 eV with sulfide interference removed), d.) tricolor map where red = oxidized sulfide, blue = sulfate, and green = sulfide, purple is where both sulfate and oxidized sulfide co-occur; e.) XANES of micrite and crinoid fragments labelled in b. XANES 1, 3 and 5 are the end-member XANES used to perform fitting, generating maps at the exact energies corresponding to the maximum intensity. Dashed lines at 2472 and 2482 represent the approximate white line of sulfide and sulfate, respectively.

Fig. 6 – Fe (left) and Mn (right) energy maps of intra-hermal sample, Lousy Cove Member, Anticosti Island in Fig. 4a.

Fig. 7 – Schematic of lithification and early marine diagenesis. a.) schematic of the water column and sediment with redox zones, concentration of sulfide (yellow) and sulfate (red) in the sediment, and locations of carbonate and pyrite precipitation (modified from Fike et al., (2015). b.) Schematic thin sections depict the evolution of carbonate components at each location shown in (a) and an example of sulfate abundance within carbonate components that we anticipate are being formed in each time interval. Abbreviations as in previous figures, PYR = pyrite, CR = crinoid, BC = bioclast, M = micrite, RU = Rugose, B = brachiopod, DR= drusy cement, BL = blocky cement, SO = syntaxial overgrowth, ME = micrite envelope, MB = micritized bioclast. Thin section 1 illustrates lithification around primary biogenic calcite and micrite lithoclasts, with initial drusy cement forming in the high SO_4^{2-} region of the sediment. An example of the anticipated high CAS abundance primary carbonate and cement is shown in a brachiopod and

drusy cement from the Hogklint Formation, Gotland. Thin section 2 shows the formation of drusy and syntaxial cements and pyrite, as well as recrystallization and micritization of fossils during early marine diagenesis. An example of low CAS abundance cement is shown in a fossilized rugose coral and micritic bioclasts from the Lousy Cove Member, Anticosti Island.

ACCEPTED MANUSCRIPT

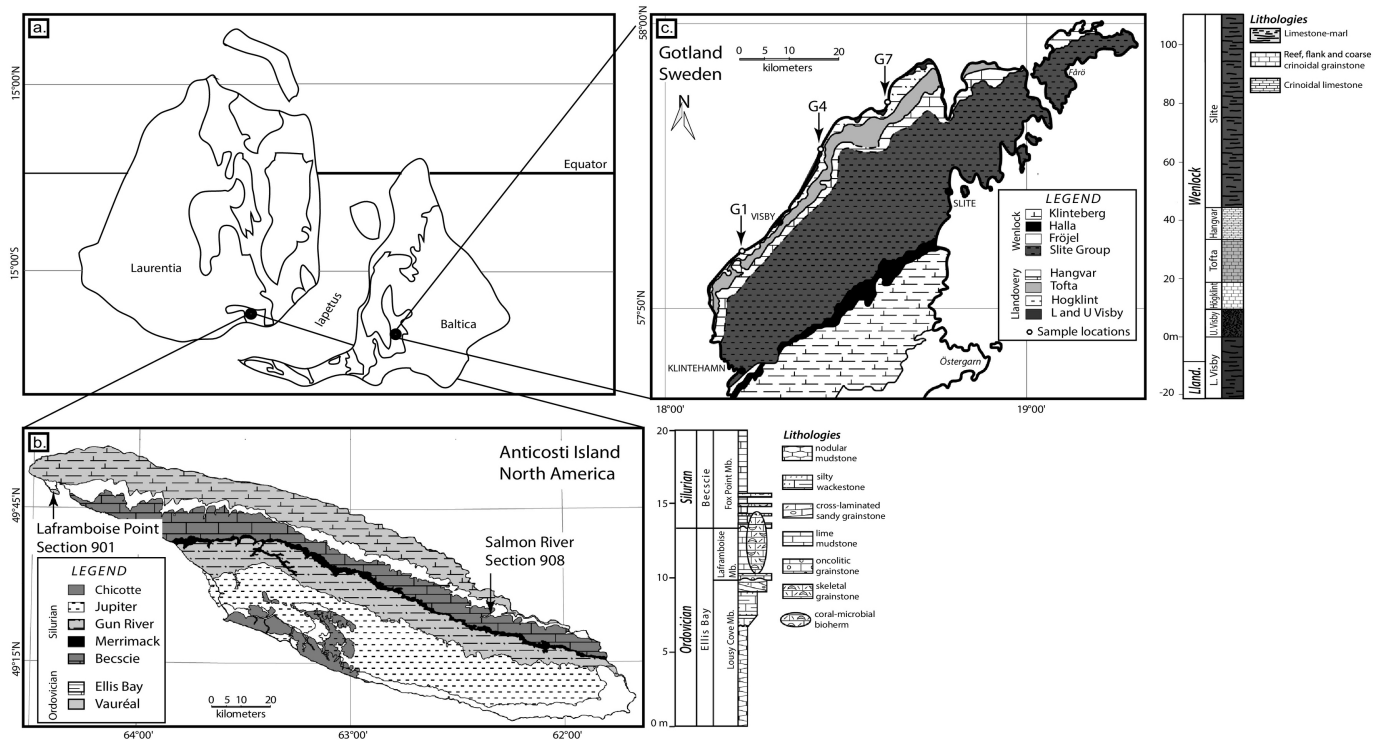


Figure 1

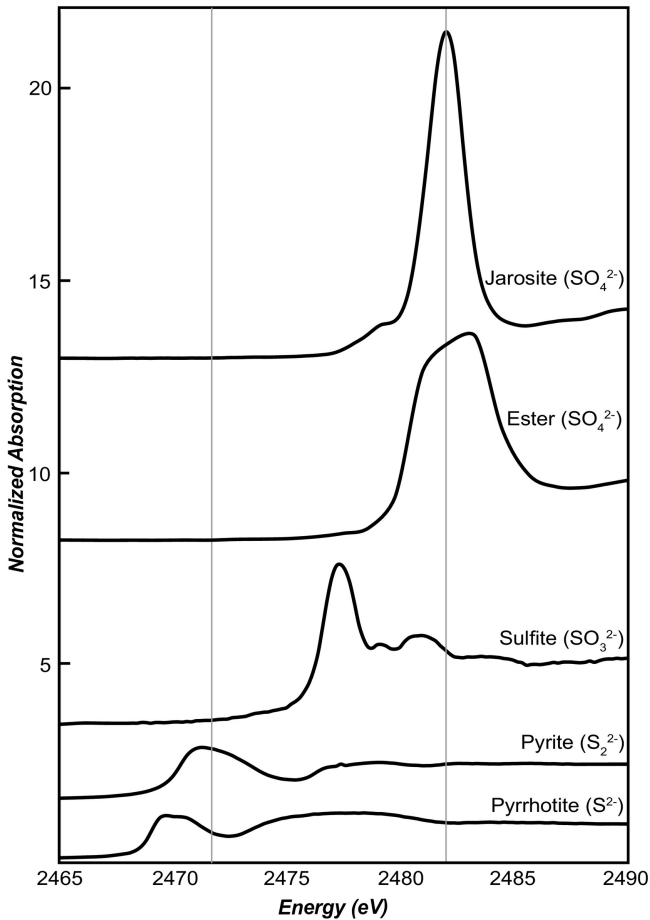


Figure 2

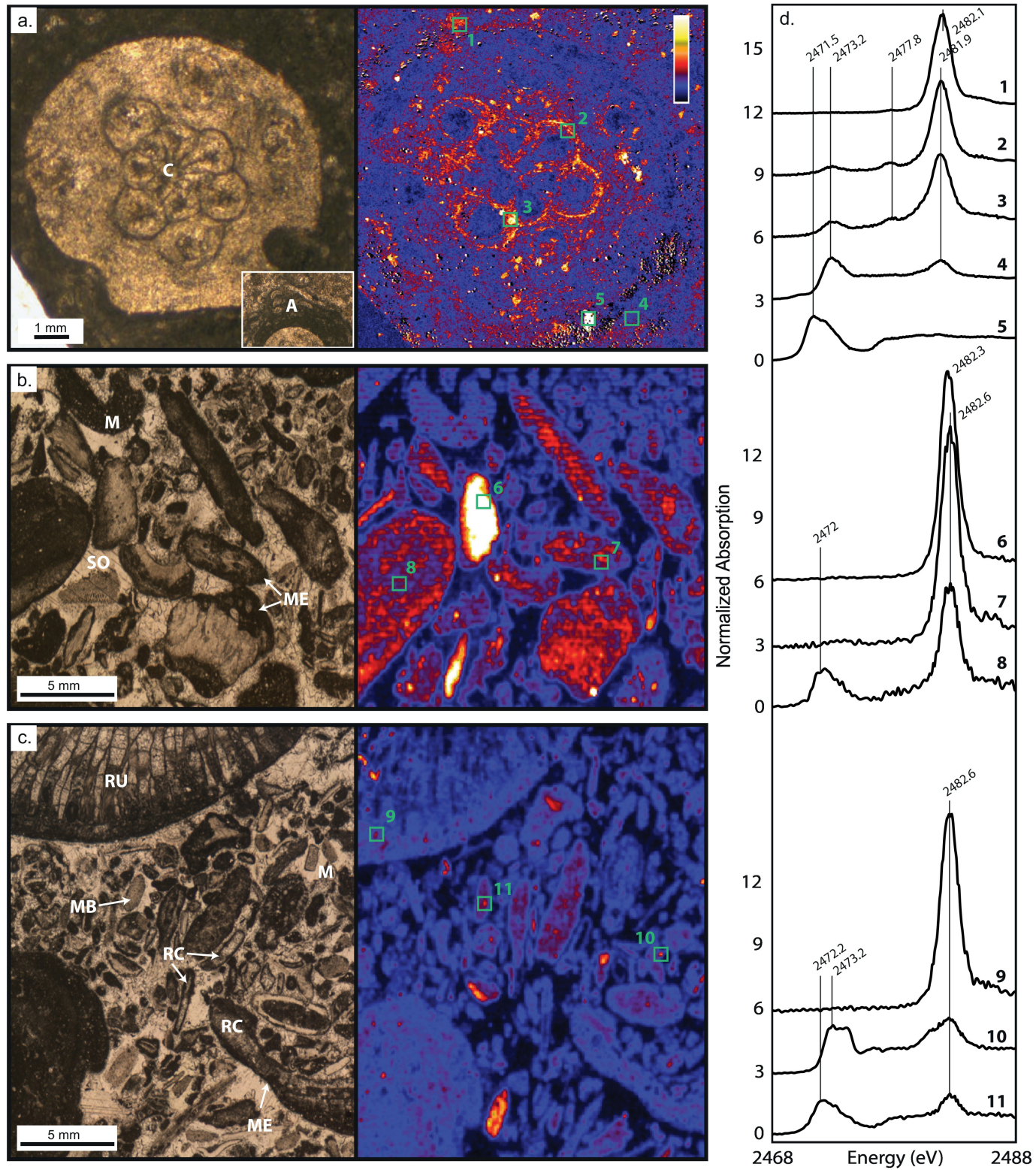


Figure 3

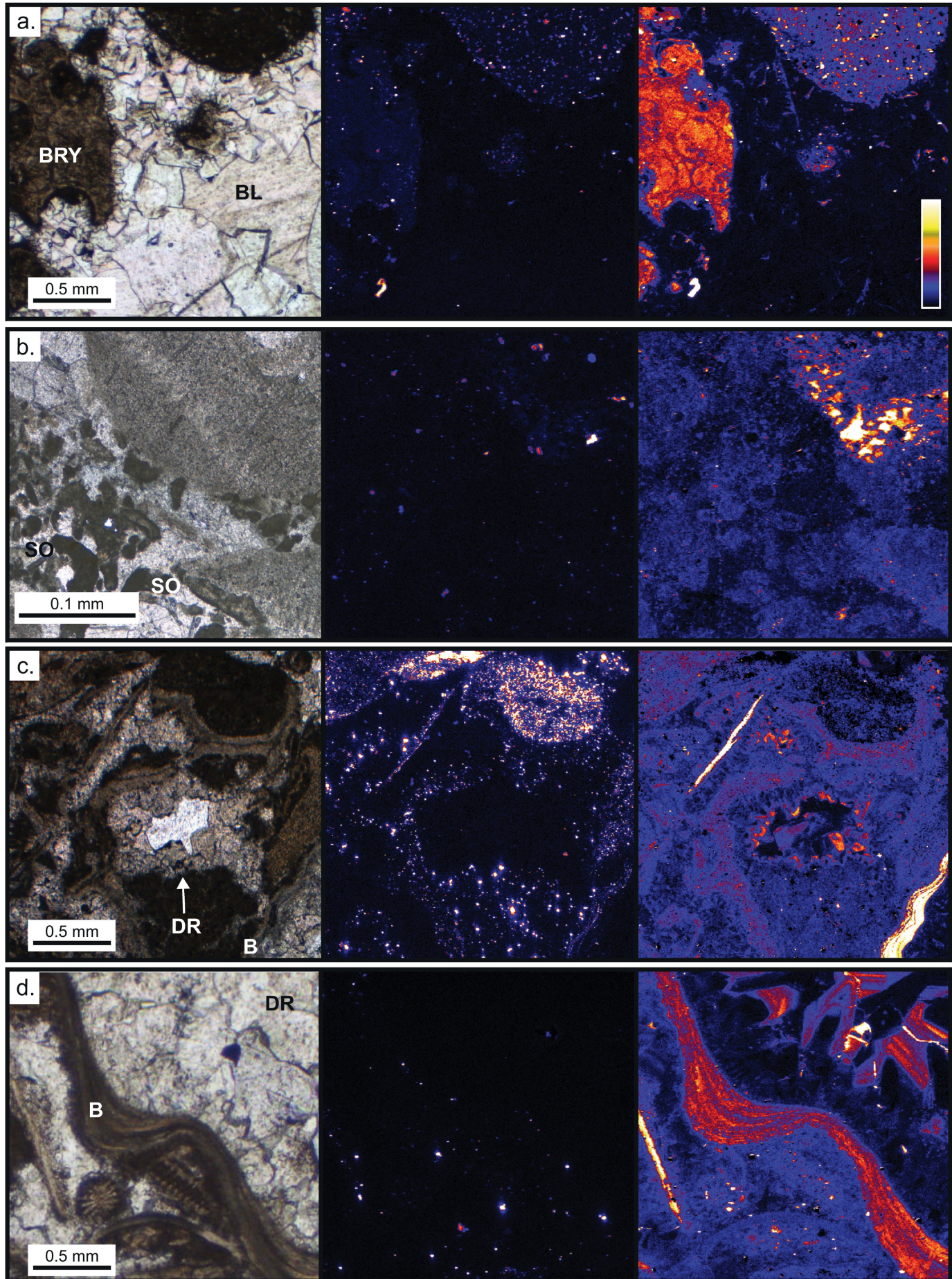


Figure 4

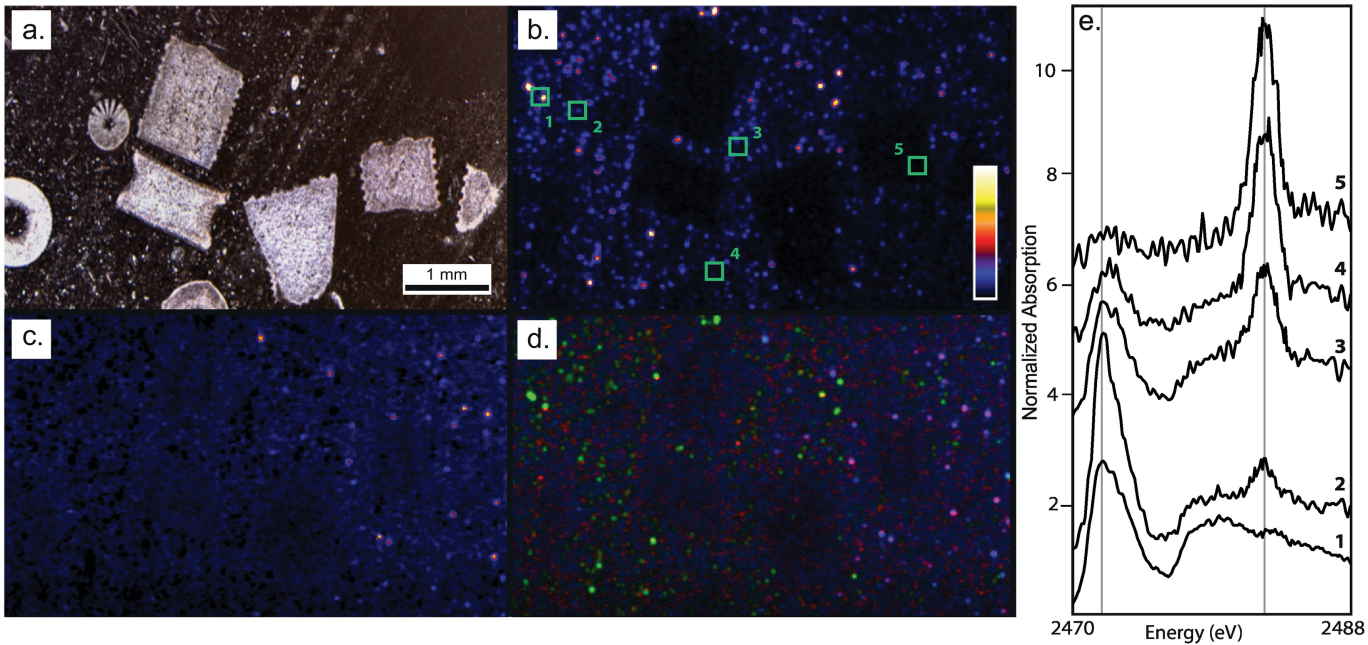


Figure 5

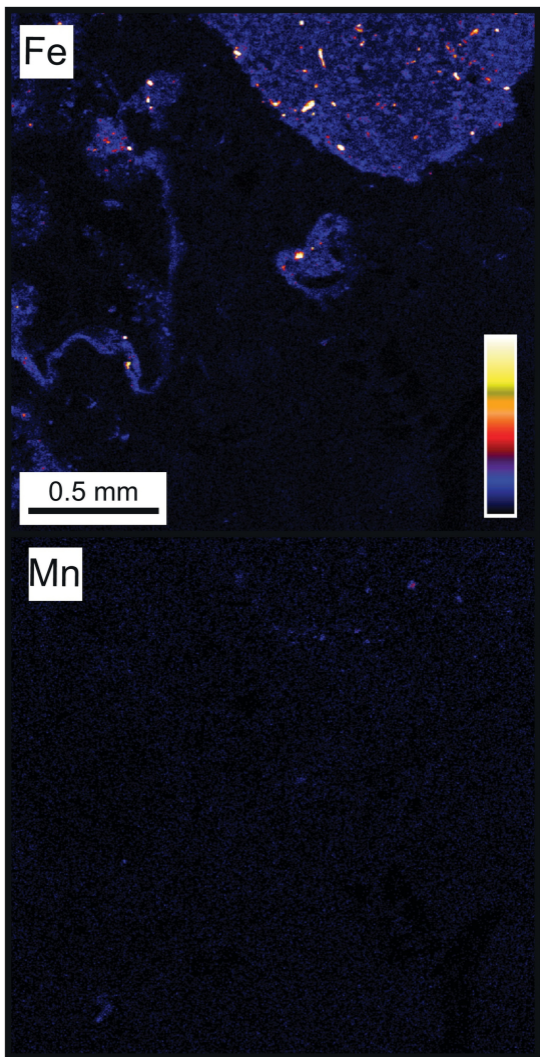
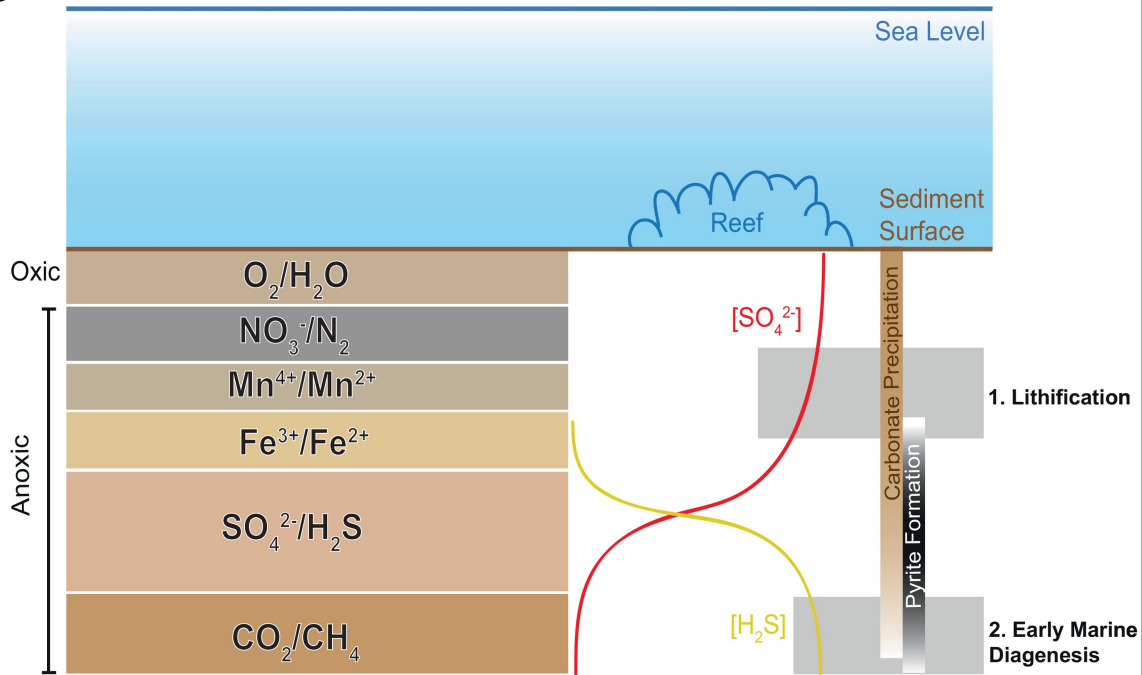


Figure 6

a. Schematic of Stratified Sediments



b. Example thin sections & anticipated sulfate abundance

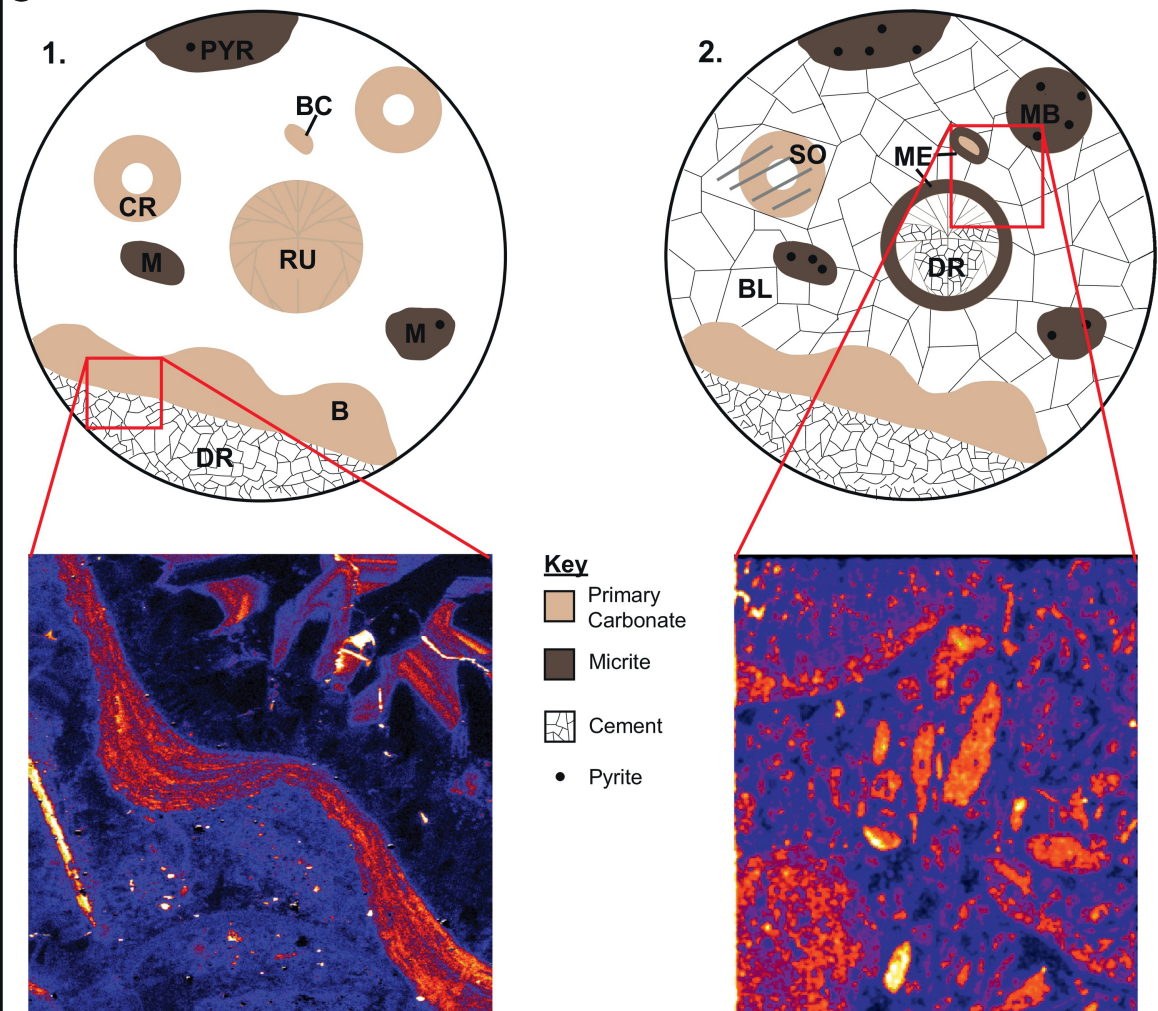


Figure 7